REPORT DOCUMENTATION PAGE

Form Approved
OMB No. 0704-0188

PLEASE DO NOT RETURN YOUR FORM TO THE ABOVE ORGANIZATION.

1. REPORT DATE *(DD-MM-YYYY)*	2. REPORT TYPE	3. DATES COVERED *(From - To)*
29-02-2008	Final	April 2006 - November 2007

4. TITLE AND SUBTITLE
Numerical Study of Unsteady Low-Reynolds Number Wing Performance

5a. CONTRACT NUMBER
-

5b. GRANT NUMBER
FA9550-06-1-0265

5c. PROGRAM ELEMENT NUMBER
-

6. AUTHOR(S)
Gopalarathnam, Ashok and McGowan, Gregory, Z.

5d. PROJECT NUMBER
-

5e. TASK NUMBER
-

5f. WORK UNIT NUMBER
-

7. PERFORMING ORGANIZATION NAME(S) AND ADDRESS(ES)
North Carolina State University
Attn: Matt Ronning, Associate Vice Chancellor, Research Administration/SPARCS
2701 Sullivan Drive, Admin Services III; MS 7514,
Raleigh, NC 27695-7514

8. PERFORMING ORGANIZATION REPORT NUMBER
-

9. SPONSORING/MONITORING AGENCY NAME(S) AND ADDRESS(ES)
Dr. John Schmisseur NA
AFOSR
875 N. Randolph Street
Suite 324, Room 3112,
Arlington, VA 22203-1768

10. SPONSOR/MONITOR'S ACRONYM(S)
AFOSR

11. SPONSOR/MONITOR'S REPORT NUMBER(S)
AFRL-SR-AR-TR-08-0162

12. DISTRIBUTION/AVAILABILITY STATEMENT
-
Approved for public release,
distribution unlimited

13. SUPPLEMENTARY NOTES
Research performed in collaboration with Dr. Michael Ol, AFRL/VAAA and Prof. Jack Edwards, NCSU

14. ABSTRACT

Unsteady motions of airfoils at low Reynolds numbers were studied computationally using low-order vortex lattice methods and using two high-order methods: a Reynolds Averaged Navier-Stokes code and an Immersed Boundary method. Results from the low-order methods compared well with experimental and computational results in the literature for small reduced amplitudes and frequencies. The high-order methods were compared with experiments on high intensity pitch and plunging motions at Reynolds numbers of 10,000 and 40,000. The pitch (rotation about the quarter chord) and plunge motions were at reduced frequencies of 3.93 and with kinematically equivalent amplitudes of effective angle of attack at the quarter-chord location. For the plunge cases, agreement between computation and experiment was qualitatively excellent and quantitatively acceptable, but for the pitch cases, the wake structure in the experiment was markedly different from that predicted by both computations, which were however similar among one another. In all cases, Reynolds number effects were found to be negligible. On-going research aims to determine the parameters necessary for pitch-plunge equivalence and also resolve the poor experiment-computation agreement for pitch.

15. SUBJECT TERMS
Unsteady aerodynamics, Airfoil, Computational aerodynamics, Experimental aerodynamics, Low Reynolds number

16. SECURITY CLASSIFICATION OF:			17. LIMITATION OF ABSTRACT	18. NUMBER OF PAGES	19a. NAME OF RESPONSIBLE PERSON
a. REPORT	b. ABSTRACT	c. THIS PAGE			Ashok Gopalarathnam
U	U	U	UU	36	19b. TELEPHONE NUMBER *(Include area code)* 919-515-5669

Final Report prepared for

Air Force Office of Scientific Research

on AFOSR Grant # FA9550-06-1-0265

Project Title:

Numerical Study of Unsteady Low-Reynolds Number Wing Performance

Principal Investigator:

Ashok Gopalarathnam
Department of Mechanical and Aerospace Engineering
North Carolina State University
Raleigh, NC 27695

Authors:

Ashok Gopalarathnam and Gregory Z. McGowan
Department of Mechanical and Aerospace Engineering
North Carolina State University
Raleigh, NC 27695

Collaborators:

Michael V. Ol (AFRL/VAAA) and Jack R. Edwards (NCSU)

Program Manager:

Dr. John Schmisseur
U.S. Air Force Office of Scientific Research

29 February 2008

Contents

List of Figures

1 Executive Summary

The main objective of this grant was for North Carolina State University (NCSU) researchers, primarily, Prof. Gopalarathnam, as PI, and Mr. Greg McGowan, as Ph.D. student, to collaborate with and provide support to the In-house Development Program (IDP) of Dr. Michael Ol of the Air Vehicles Directorate of the Air Force Research Labs (AFRL/VAAA) in his efforts in the area of low-Reynolds number unsteady aerodynamics of airfoils and wings. The goals of the NCSU effort were to develop an approach using analytical and computational tools, ranging from low-order unsteady panel methods to higher-order Reynolds Averaged Navier-Stokes codes, for analysis of unsteady motions of low-Reynolds number airfoils and wings. The long-range vision is that such an approach can eventually be used to study gust response of micro air vehicles and design controllers for such vehicles. An important objective of the effort was also to compare the computational results from the NCSU effort for unsteady motions of airfoils with anticipated results from experimental studies that were being conducted by Dr. Michael Ol in the Horizontal Free-Surface Water Tunnel (HFWT) at AFRL as a part of his IDP effort.

The accomplishments made under this effort can be most easily described when classified chronologically into three phases. An overview of the accomplishments under each phase are described in the paragraphs below.

1.1 Overview of Accomplishments during Phase 1

In the first phase of the effort, which lasted approximately one year, the primary objective was to develop an unsteady numerical thin-airfoil theory code, UnsTAT, for rapid analysis of unsteady motions of airfoils and trailing-edge flaps. This code was developed and the results were compared with experimental and numerical results from the literature. The code and results are described in detail in Sec. 2. The objective behind the development of this code was that, after suitable calibration with results from higher-order methods and experimental results, it could be used in vehicle modeling and control.

Towards the end of this phase, the interest in the collaborative effort shifted towards developing a better understanding of the fundamental flow physics of low-Reynolds numbers undergoing high intensity unsteady motions. This change in interest led to the activities of Phase 2.

1.2 Overview of Accomplishments during Phase 2

With the HIPPO (High-Intensity Pitch Plunge Oscillations) experimental investigations[1] of Dr. Ol in the HFWT water tunnel gaining momentum, it was felt that the collaborative effort between NCSU and AFRL would be better served by focusing on computational studies of pure-plunge and pure-pitch (rotation about the quarter-chord location) motions to be studied in HFWT experiments. Reynolds numbers of 10,000 and 40,000 were chosen as representative values. The two computational approaches were compared for capacity to resolve shed vortical structures near the airfoil and in the wake, and for capacity to resolve the mean streamwise momentum balance in the wake. The plunge and pitch were each at reduced frequency, k = 3.93, and with kinematically equivalent amplitudes of effective angle of attack to see if they would result in similar flow structures in the wake.

Because of the high reduced amplitudes and reduced frequencies involved, the focus of the compu-

tations was on the use of high-order RANS methods. The CFL3D code from NASA Langley was used because of previous experience with this code.[2] In addition, because Prof. Jack Edwards of NCSU was developing immersed boundary (IB) methods, which are well suited for the study of unsteady motions, the authors sought the collaboration of Prof. Edwards in using his IB code as a second computational method. With the involvement of Prof. Edwards, the collaborative effort led to comparison between two sets of computations with the experimental results from AFRL. The results of this computation-experiment comparison were published as a paper[3] at the 46^{th} AIAA Aerospace Sciences Meeting in January 2008.

For the plunge cases, agreement between computation and experiment was qualitatively excellent and quantitatively acceptable, but for the pitch cases, the wake structure in the experiment was markedly different from that predicted by both computations, which were however similar among one another. In all cases, Reynolds number effects were found to be negligible. Experimental-computational agreement for plunge, but lack of agreement for pitch, is presently left unresolved.

One of the major questions arising from the computation-experiment comparison in this phase was: For airfoil motions, is there a pure-pitch motion, defined by reduced amplitude and pivot-point location, that will produce the same $C_l(t)$ and possibly $C_m(t)$ as a plunge motion of given reduced amplitude and frequency? The focus of the third phase, which is an on-going effort towards the Ph.D. research of Mr. McGowan, is to attempt to answer this question.

1.3 Overview of Accomplishments during Phase 3

The on-going phase-3 effort attempts to find equivalence between pitch and plunge motions for an airfoil. To start with, motions of small reduced frequency and amplitude are being studied using Theodorsen's theory in an attempt to analytically determine an equivalence between pure-pitch and pure-plunge motions. Early results show promise for this effort. If this effort is successful, the next step will involve use of low- and high-order computational methods and experiments to verify the findings and to extend the equivalence to higher frequencies and amplitudes.

The remainder of the report provides a detailed description of the approaches, results, and interim conclusions of the three phases in Sections 2, 3, and 4. The summary and conclusions along with future directions for the research are described in Sec. 5.

2 Phase 1 Accomplishments

An early objective of the NCSU research in the collaboration with AFRL was in developing an approach that integrates the use of low-order numerical models using unsteady panel or vortex-lattice methods with high-order analyses using RANS CFD codes for time-accurate computations. While the high-order modeling using RANS codes will provide high-fidelity solutions that have potential capture the details of the flow phenomena, they are computationally very intensive and are not amenable to use in flight dynamic analysis and control-law development. The low-order modeling using unsteady panel methods, on the other hand, will not be able to resolve flowfield details, but is often adequate for determining the global aerodynamics such as time-varying lift and pitching moment. For this reason low-order modeling using rapid, simple models needs to be investigated in parallel with the high-order modeling. When sufficient insight is available from experiments and unsteady RANS, it is possible to judiciously use the low-order methods for rapid evaluation of flight dynamics, simulation, and control-law development.

The effort during Phase I focused on development of a numerical unsteady thin airfoil theory (UnsTAT) code, that is described in the following subsections.

2.1 UnsTAT

Following the discrete vortex method described in Ref. 4, UnsTAT utilizes thin-airfoil theory to simulate steady-state solutions at each timestep. A shedding of discrete vortices is used to approximate the trailing wake at each timestep. At each step the typical boundary conditions of zero normal flow through each panel are applied along with the Kelvin condition, Eqn. 1. This leads to an influence coefficient matrix which can then be used to determine the circulation on all panels as well as the strength of the latest shed vortex, Γ_{W_t}. More details of the method are described in textbooks such as Ref. 4.

$$\Gamma(t) - \Gamma(t - \Delta t) + \Gamma_{W_t} = 0 \tag{1}$$

2.2 UnsTAT Validation

2.2.1 Step increase in angle of attack

In this subsection, the results for a 8.4%-thick symmetric von Mises airfoil in uniform freestream undergoing a step increase in angle of attack from 0 to 0.1 radians are examined. The analytical result used for comparison is the R. T. Jones approximation to the Wagner function, as shown in the Ph. D. thesis of Young.[5] This analytical result is also discussed in Fung.[6]

$$\frac{C_l}{C_{l_{(t=\infty)}}} = 1 - 0.165e^{-0.0455\tau} - 0.335e^{-0.300\tau} \tag{2}$$

where

$$\tau = \frac{2Ut}{c}$$

Also included, in addition to analytical results, are the results from Young's unsteady panel method[5] (UPM), and results from the numerical analysis of Basu et. al.[7] Figure 1 shows the progression of lift with time for a flat plate at angle of attack. In this figure, at the instant $\frac{U_\infty t}{c} = 0.0$, the airfoil is pitched up to an angle of attack of 0.1 radians. It is seen that the UnsTAT code matches the analytical result from the Wagner function quite well. The small offset between results obtained with the UnsTAT code and those obtained from Young's UPM[5] and Basu's code[7] is due to thickness effects, as UnsTAT and the analytical results assume a flatplate for the analysis while results from Young as well as Basu were computed for an 8.4% thick von Mises airfoil.

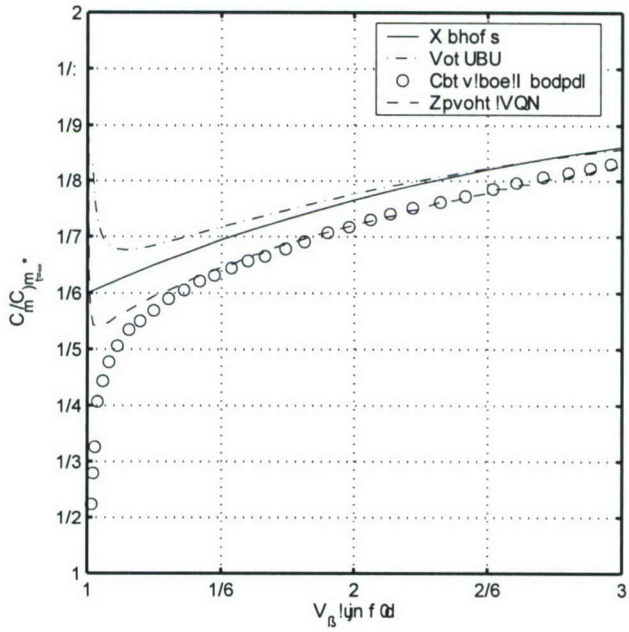

Figure 1: Lift variation with time for an 8.4%-thick symmetric von Mises airfoil undergoing a step increase in angle of attack of $\alpha = 0.1$ radians at $t = 0$.

2.2.2 Pitching motions at moderate frequency

In this subsection, the results from UnsTAT code and the CFL3D RANS code (discussed later in Sec. 3.3.1) are compared with those from the experimental data set of Piziali.[8] Although this data set is extensive, two particular cases were chosen for exploration. The first case is a fully-attached case in which the motion is described by $\alpha(t) = 4 + 4sin(\omega t)$. This case was chosen because of its "cleanliness" or lack of separation regions near the leading and trailing edges. Therefore, the assumption of the Kutta Condition, applied at the trailing edge in the UnsTAT code, is a good one. In the second case the motion is described by the equation: $\alpha(t) = 11 + 4sin(\omega t)$. For this case the flow does indeed separate at the higher angles of attack, which invalidates the assumptions made in the UnsTAT code. This is also a more complicated case, especially for the UnsTAT code, to predict and therefore the comparison is expected to be poor.

Figure 2 shows the results for the first case, $\alpha(t) = 4+4sin(\omega t)$, in which the flow remains attached throughout the range of motion. It can be seen that for lift, drag, and moment coefficients, Figs. 2 (a), (b), and (c), respectively, the CFL3D code does a very good job in predicting the overall

performance. There are, however, some slight differences in the magnitude of the drag coefficient, but the shape of the hysteresis loop is very closely predicted. UnsTAT predicts the lift coefficient, Fig. 2 (a), very well, but does a poor job predicting the drag coefficient, Fig. 2 (b). This can be expected for a potential method in which viscous effects are neglected altogether. The moment coefficient, Fig. 2 (c), similar to drag, is not accurately predicted by UnsTAT.

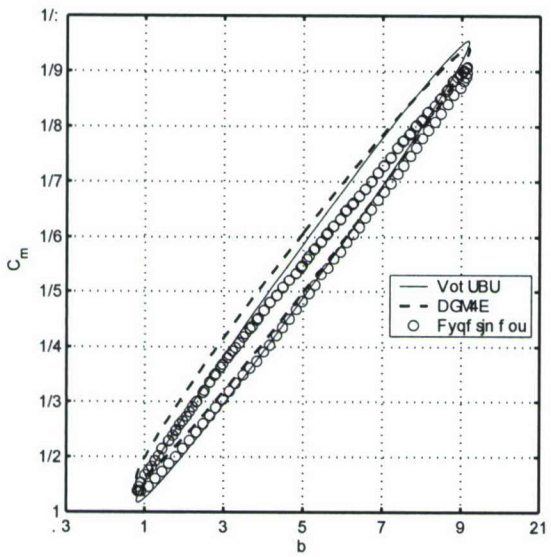

(a) C_l vs. Alpha

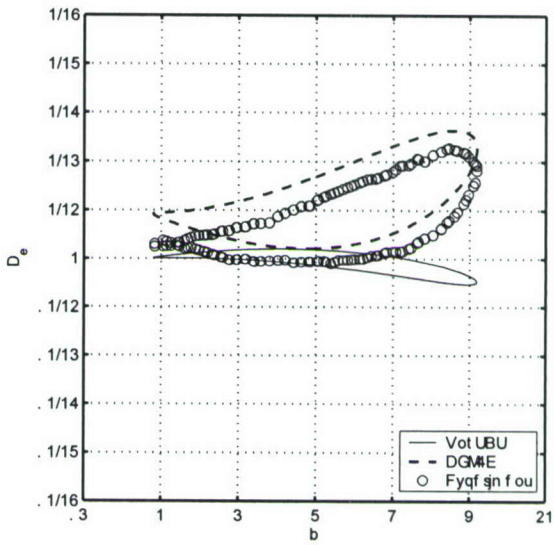

(b) C_d vs. Alpha

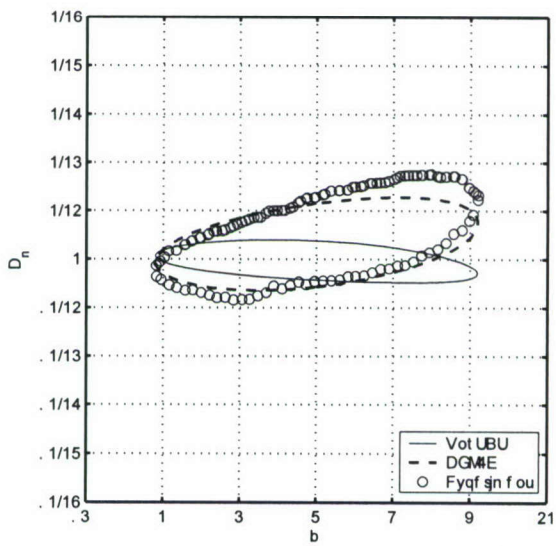

(c) $C_{m_{c/4}}$ vs. Alpha

Figure 2: Lift, Drag, and Moment hysteresis loops, $\omega = 0.001$, $\alpha(t) = 4 + 4sin(\omega t)$.

Figure 3 shows the results for the second case, $\alpha(t) = 11 + 4sin(\omega t)$, in which the flow separates close to the upper limits of angle of attack. Here as expected, the UnsTAT code fails to accurately predict the airfoil performance. Since UnsTAT is not capable of handling flow separation, the lift, shown in Fig. 3 (a), is over predicted for all angles of attack. By a similar accord, the drag, shown

in Fig. 3 (b), is underpredicted for all angles of attack. The CFL3D results show good comparison in drag and moment coefficients, Figs. 2 (b) and (c), during the upstroke of the airfoil. The lift coefficient, Fig. 2 (c), is overpredicted for the entire sequence of angles of attack.

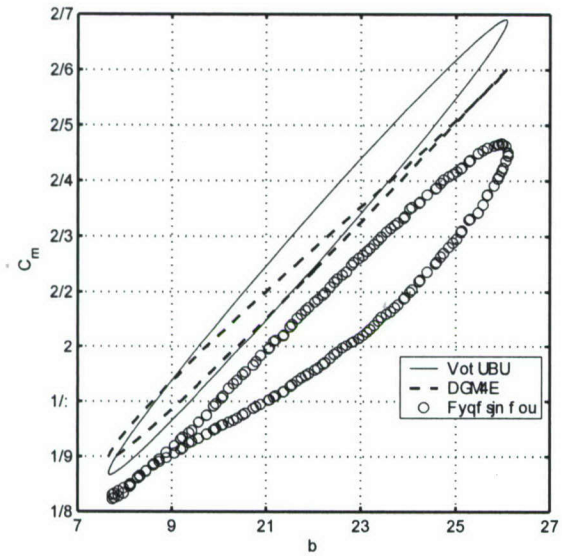

(a) C_l vs. Alpha

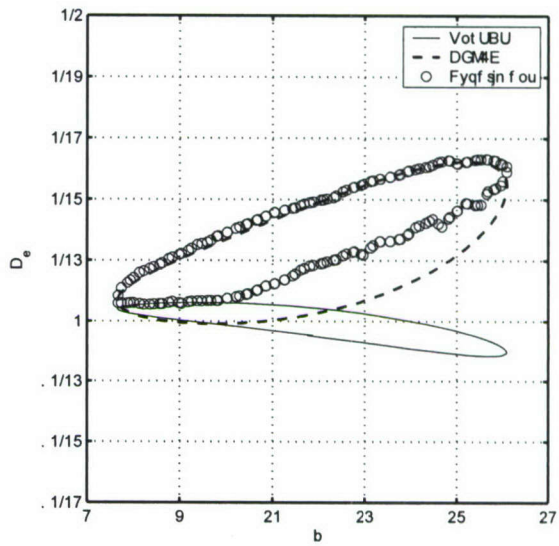

(b) C_d vs. Alpha

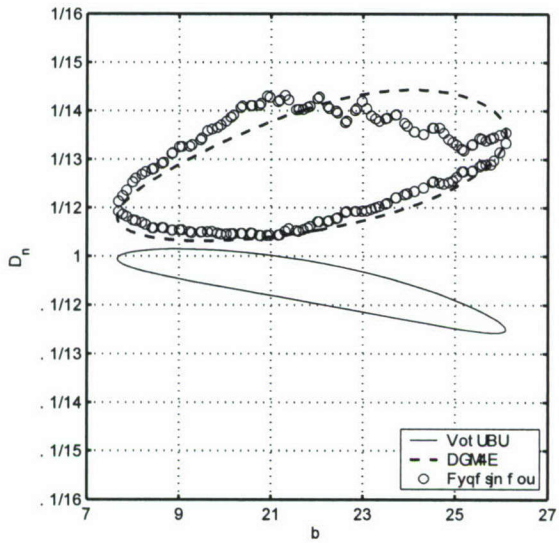

(c) $C_{m_{c/4}}$ vs. Alpha

Figure 3: Lift, Drag, and Moment hysteresis loops, $\omega = 0.001$, $\alpha(t) = 11 + 4sin(\omega t)$.

2.2.3 Plunging motion at moderate frequency

For validation of plunging motions, two cases were extracted from Ref. 5. The cases vary in both plunging frequency and plunging amplitude of a symmetric airfoil (NACA 0012). For each case, the UnsTAT code is compared to both an inviscid run utilizing CFL3D and Young's UPM.[5] The

Young's UPM[5] follows a method which is similar to that of Basu and Hancock.[7] While UnsTAT approximates the airfoil as it's camberline, a flat plate for symmetric airfoil, both the results from Ref. 5 and CFL3D include thickness effects.

Figure 4 shows the results for the plunging airfoil undergoing the following motion: $y(t) = 0.15cos(2.0t)$ and Fig. 5 shows the results for the plunging airfoil undergoing the following motion: $y(t) = 0.0375cos(8.0t)$. It can be seen that for both cases the results from each code match very well.

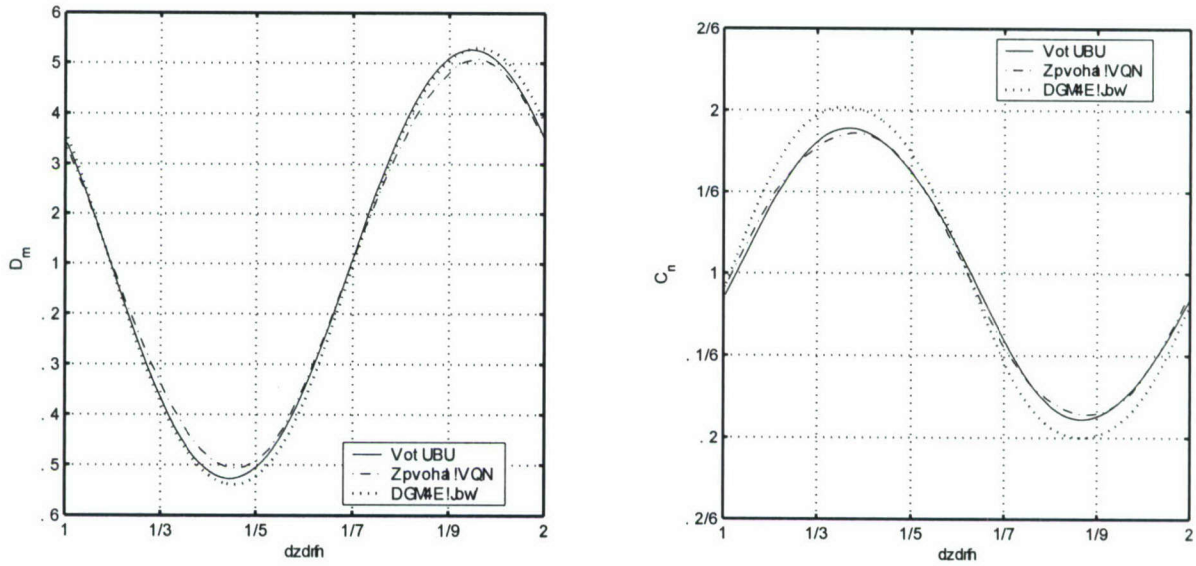

(a) C_l vs. Cycle

(b) C_m vs. Cycle

Figure 4: Lift and Moment coefficient variation with time, $\omega = 2.0$, $h = 0.15$.

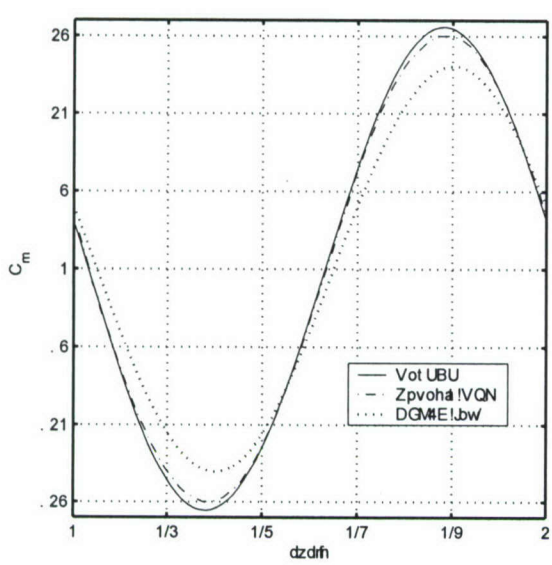

(a) C_l vs. Cycle

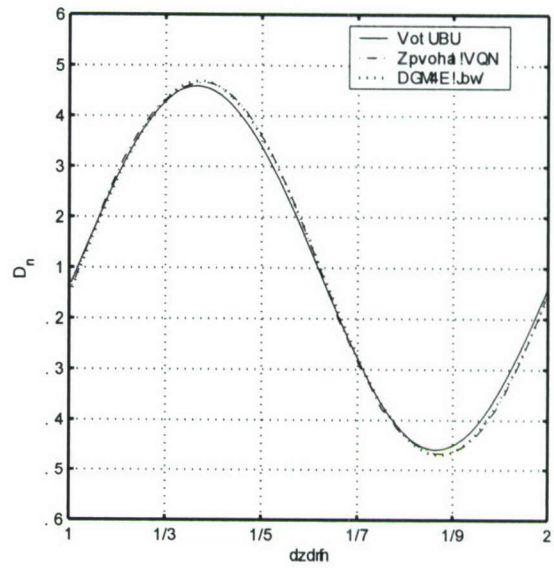

(b) C_m vs. Cycle

Figure 5: Lift and Moment coefficient variation with time, $\omega = 8.0$, $h = 0.0375$.

2.3 Summary for Phase 1

An Unsteady Thin-Airfoil Theory (UnsTAT) code was developed in Phase 1. After the development of the UnsTAT code, an assessment of its capability was made. The assessment included comparisons to three types of motions: i) instantaneous angle of attack change, ii) pitching motions at moderate frequencies, and iii) plunging motions at moderate frequencies. The results indicate that for small reduced frequencies, the UnsTAT code is sufficient for calculating lift and moment values. As expected, for flows with large separated regions or flows with high reduced frequencies, the UnsTAT code does a poor job predicting the loads on the given geometry.

3 Phase 2 Accomplishments

With the High-Intensity Pitch Plunge Oscillations (HIPPO) experiments of Dr. Michael Ol gaining momentum, it was decided that the AFRL-NCSU collaborative research effort would be most beneficial if the NCSU effort focused on computational studies of the motions to compare with results from the experimental investigations at AFRL. This section describes the computation vs. experiment for the pitch/plunge motions of an airfoil at low Reynolds numbers.

Much of this section was adapted from the joint paper[3] authored with Dr. Michael Ol of AFRL, Prof. Jack Edwards of NCSU, and Mr. Daniel Fredberg of the Air Force Institute of Technology.

3.1 Introduction

Pitch and plunge of airfoils are useful and common abstractions in unsteady aerodynamics for a wide range of applications in low-speed flight. The motivation of the present work, and the point

of departure from classical unsteady airfoil theory[9] and classical dynamic stall,[10] is aerodynamic modeling for Micro Air Vehicles (MAVs) of all three types — fixed-wing, rotary-wing, and flapping-wing. The small size and low flight speed of MAVs necessarily leads to high dimensionless rates of motion, either intentional (aggressive maneuver, wing rotation for "perching", high reduced-frequency wing flapping) or unavoidable (gust response). Large reduced frequencies and large excursion amplitudes in angles of attack raise basic questions regarding the degree of unsteadiness of the encountered flowfields, and how the aircraft — presently, abstracted to a 2D airfoil — will respond to time-varying angle of attack. Matters are further complicated by laminar separations at low Reynolds number, where even in the steady case one finds unusual behavior in $C_L = f(\alpha)$.[11] One basic question is the extent of quasi-steadiness: when is lift coefficient linear with time-varying angle of attack? Beyond the limited scope of quasi-steady problems, is there a reliable truncation of Taylor expansion in angle of attack, with constant coefficients — that is, when is it reasonable to write: $C_L(t) = C_{L_o} + C_{L_\alpha}\alpha + C_{L_{\dot\alpha}}\dot\alpha$? In what cases can the lift coefficient response be approximated as an nth-order linear system?[12] And for example for the case of large-amplitude and high-frequency airfoil pitch, does "angle of attack" even have a well-defined meaning?

This phase of the work began by considering experiment vs. computation for benchmark results in the unsteady airfoil literature. The choice of reduced frequency was motivated by NACA0012 pure-plunge experiments of Lai and Platzer,[13] where the focus was on thrust-production and wake structure for various combinations of reduced frequency and reduced amplitude. The MAV application, where $C_L > 0$ is important, suggests a cambered airfoil with good on-design performance at MAV-relevant Reynolds numbers; the Selig SD7003 airfoil[14] was chosen because of prior work on the static case.[15] Plunging motion would therefore be defined as $h(t) = h_o cos(2\pi ft)$ with resulting angle of attack time history $\alpha(t) = \alpha_o + arctan\left(2\pi fch(t - \frac{\pi}{2})/U_\infty\right) = \alpha_o + arctan\left(2kh(t - \frac{\pi}{2})\right)$ and maximal extent of angle of attack of $\alpha_T = \alpha_o \pm arctan\,(2kh_o)$. The pure-pitch case, meanwhile, is given by $\alpha_T(t) = \alpha_o + \theta_o cos\,(2\pi ft + \phi)$. In pitch and plunge the offset angle α_o and the motion frequency, f, are taken to be the same. Further, we choose $\theta_o = arctan\left(2kh(t - \frac{\pi}{2})\right)$ to equate the kinematic pitch amplitude with the plunge-induced alpha amplitude — as suggested in the dynamic stall literature[10] and classical results for unsteady airfoil response, if the angle of attack time-derivative term is neglected.[16] Following a plunge-case studied by Lai and Platzer,[13] we take $k = 3.93$ (note the factor of 2 difference in definition of k) and $h = 0.05$. With $\alpha_o = 4°$, this gives $\alpha_T = 4° \pm 21.5°cos(2\pi ft)$.

Besides direct comparison of pitch and plunge, and some mention of Reynolds number effects, this effort seeks to mutually validate the experiment and computation. For computations, the objective is to benchmark two different approaches — one a commonly used RANS code, and the other an extension of immersed boundary methods. In both cases the usual issues of turbulence model, capture of transition in boundary layers and shear layers, wall effects and grid/temporal resolution are considered. On the other hand, the computations facilitate a sort of validation of the experiment, concerning issues such as blockage in the test section, interference of the model support structure, effects of the free-surface in the water tunnel test section, effects of facility flow quality, kinematic accuracy of the motion rig and near-wall resolution limits of the particle image velocimetry dataset.

3.2 Experimental Details

Experiments were conducted in the Air Force Research Laboratory's Horizontal Free-surface Water Tunnel ("HFWT"); the HFWT and the approach used for airfoil PIV measurements are described

in Ol et al.[15] PCO 4000 11Mpix cameras were triggered off of an external pulse train derived from the position encoder of the motion rig, thus allowing for selection of motion phase at which to acquire data. Airfoil motion was driven by a 2-degree-of-freedom "pitch-plunge rig", consisting of a pair of electric linear motors mounted vertically on a plate above the tunnel test section free-surface. Each motor actuates a vertical rod, which connects via a bushing to the airfoil at a fixed pivot point on the airfoil chord. Motion trajectory of each rod is programmed independently, allowing for single degree-of-freedom motions such as sinusoidal pure-pitch or pure-plunge, as well as nontrigonometric and combined motions. The pivot point for pitching motions can be varied as well, but for simplicity was limited in the present study to the quarter chord. Detail of the pitch-plunge rig is given in Ol.[1]

Velocity data were acquired at four phases in each period of oscillation, for a sequence of 120 periods. Prior results with dye injection and PIV for pure-pitch at $k = 3.93$ and $Re = 60,000$[1] show that startup transients relax and the flow attains periodicity in less than two periods of oscillation after startup, where the startup is continuous in velocity and bound by 5 m/s^2 in acceleration in the controller software. In the present work, the first 5 periods were removed from the data set, and the remainder was ensemble averaged for each phase of motion. Vorticity was calculated by explicit differentiation of cubic spline fits to the velocity field.[17]

Resolution ranged from 88 $pixels/cm$ to 110 $pixels/cm$. For 32×32 pixel windows with 16×16 overlap, this results in 84 to 105 vectors per chord, respectively. Because of laser reflections from the model surface (polished stainless steel, painted flat-black) and lack of corrections for PIV windows which at least partially intersect with the model surface or for pixel regions saturated due to laser reflections, data closer than one window length to the airfoil wall — approximately $0.02c$ — are not reliable. This renders problematic a direct comparison of PIV and CFD in attached boundary layers.

For $Re = 40,000$, $k = 3.93$ corresponds to a physical frequency of 2.12 Hz and tunnel flow speed of 26.5 cm/s. For $Re = 10,000$, frequency and flow speed are 4 times lower. With a 61 cm wide by 61 cm high test section, blockage based on projected frontal area of the model at maximum pitch amplitude is 9%. Gaps between the model tips and the tunnel walls were approximately 1.0 mm. To obtain the "most 2-dimensional" flowfield, the PIV light sheet was placed at the 3/4 span location; that is, approximately halfway between the plunge rods and the tunnel wall. Light sheet thickness was approximately 2 mm, though the large field of coverage (up to 45 cm) makes precise collimation of the light sheet difficult.

The installation of the model and schematic of the rig assembly are shown in Fig. 6. In the photograph, the model is inside the test section, but the glass walls are not visible.

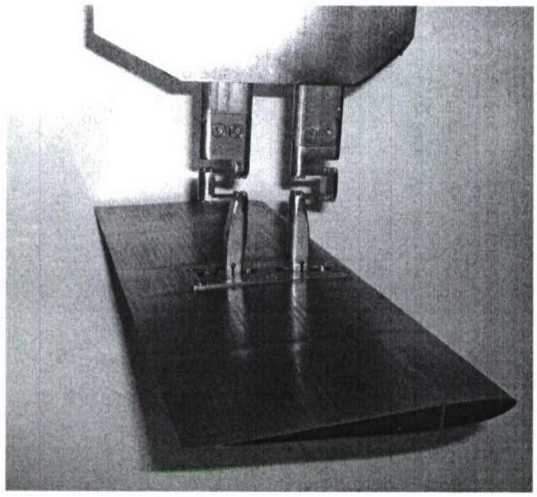

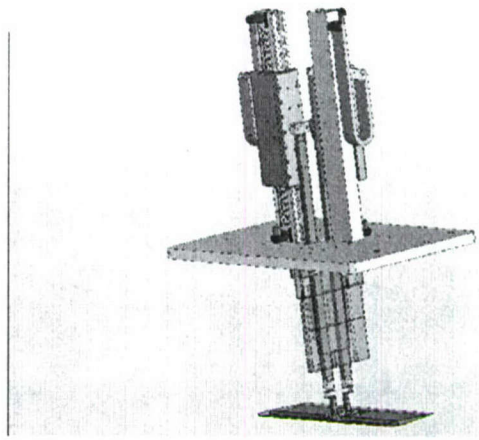

Figure 6: SD7003 airfoil installed in HFWT test section, with plunge rods in position prior to a run (left); and schematic of pitch/plunge rig and airfoil model (right).

3.3 Computational Details

3.3.1 CFL3D

CFL3D[2] is a research code developed at NASA Langley Research Center that solves the Thin-Layer Navier-Stokes equations. The CFL3D code is a robust flow solver that has been utilized by many researchers for a wide range of applications. It is written in the structured framework and is capable of calculating solutions on one-to-one, patched, or overset grids. CFL3D also includes convergence acceleration techniques, namely local time step scaling, grid sequencing, and multigrid. It also includes built in routines to accommodate grid motions, including grid deformations; with these, simple motions, such as translations and rotations, and complicated motions, such as deforming surfaces and other aeroelastic type motions, can be solved. Although several turbulence models are built into the CFL3D code the current research utilizes only the Spalart-Allmaras[18] turbulence model. Low-speed preconditioning[19] was not utilized in the current research; instead computations were run at a higher Mach number of 0.2, and computational frequency was adjusted to match the physical frequency of experiment.

For this work, two grids were used. The first grid, shown in Fig. 7, consists of 689 nodes in the i^{th}-direction (around the airfoil surface) and 113 nodes in the k^{th}-direction (normal to airfoil). A denser spacing near the airfoil surface was implemented to accurately predict boundary layer effects. The outer domains of this grid extend to approximately 20 chords radially away from the airfoil in all directions. Unsteady motions using this grid were performed utilizing the grid motion technique implemented in CFL3D.[20] In this technique the entire grid moves to simulate the respective motion. The second grid, shown in Fig. 8, was created to account for tunnel wall effects, located at $y = \pm 2c$. It consists of 441 nodes in the i^{th}-direction and 49 nodes in the k^{th}-direction.

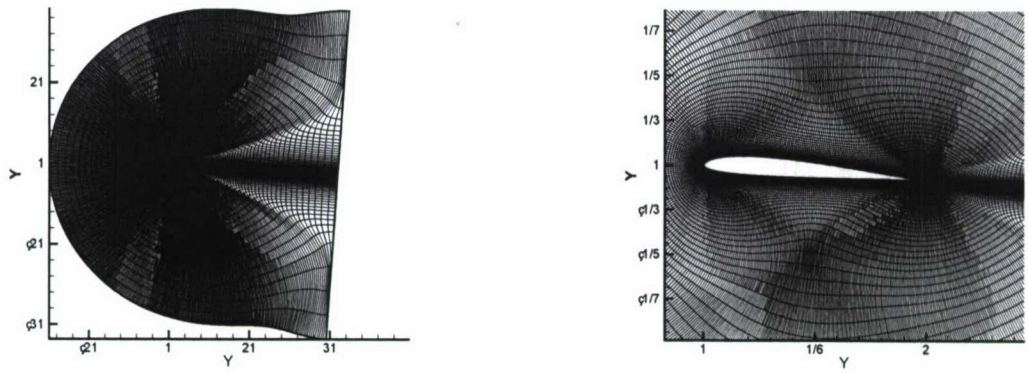

(a) Entire grid

(b) Close up

Figure 7: Schematic of grid utilized for CFL3D simulations using moving grid capability.

3.3.2 Immersed Boundary

The basic idea of the immersed boundary method is to resolve the flow features around a given geometry that has been embedded into a computational mesh without requiring that the boundary points coincide with mesh nodes. These methods can be extremely useful for complex geometries. The idea is to resolve flow around these complex bodies while avoiding the difficulties associated with grid adaptation, overset grids, or moving grids. With the immersed boundary method a designer need only a cartesian mesh along with the cloud of points that define the surface geometry. The method implemented here follows that of Mohd-Yusof,[21,22] in which the methods developed by Peskin[23] are interpreted as a direct momentum forcing. The effects of the immersed boundary are included by defining band cells, those surrounding the body, and prescribing conditions at these points. The conditions prescribed mimic the movement of the surface, shearing effect, and heat transfer. The code, developed by Choi et al.,[24] solves the incompressible Navier-Stokes equations utilizing the finite volume method; a greater detail of the coding algorithm is given in Ref. 24. The Spalart-Allmaras turbulence model was also used for the immersed boundary runs.

3.4 Results

In the following subsections the various CFD results are compared with experiment by means of streamwise velocity contour plots, vorticity contours, and wake u-momentum profiles.

3.4.1 CFL3D Grid Convergence Study

Three grid levels were examined with CFL3D to determine grid convergence. The finest grid level being comprised of 77,857 grid points, with 689 points in the streamwise directions and 113 points normal to the airfoil. The medium grid consisted of 19,665 points, with 345 in the streamwise direction and 57 normal to the airfoil. Finally the coarse grid was made up of 5,017 points, with 173 in the streamwise direction and 29 normal to the airfoil. Each of these grids was studied both in pure-plunge and pure-pitch.

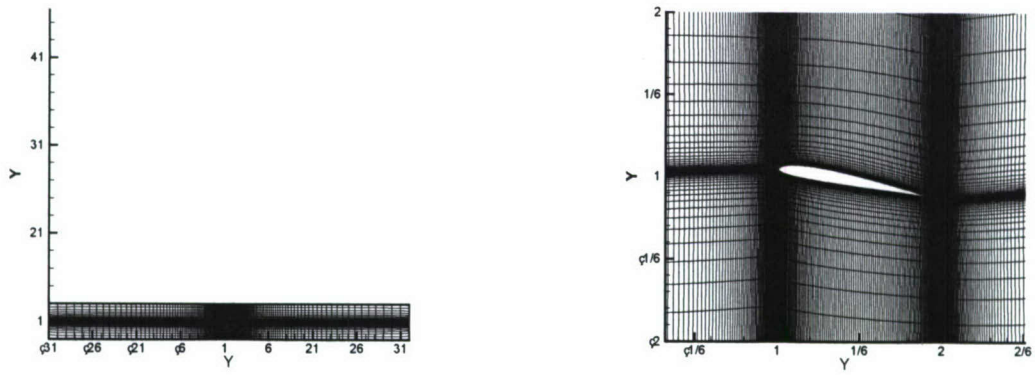

(a) Entire grid

(b) Close-up

Figure 8: Schematic of grid utilized for CFL3D simulations of pure-pitch motion using mesh deformation capability to study blockage effects.

Figure 9 gives a summary of the load history of the airfoil in pure-plunge for each grid level. Lift is given in Fig. 9 (a), drag in Fig. 9 (b), and moment, about the quarter chord, in Fig. 9 (c). From these figures it can be deduced that, in terms of airfoil loads, for the plunge case grid convergence has been achieved. Furthermore, if the loads are of interest, it would be sufficient to utilize the results from the coarse grid case, saving a tremendous amount of time in computations.

However, examining the normalized vorticity contours for the coarse, Fig. 10 (a), medium, Fig. 10 (b), and fine, Fig. 10 (c), grids we see that the vorticity is very different between the coarse grid and the fine grid. This result indicates that the grid resolution is critical in predicting the vorticity strength, particularly in the wake region. Examining Fig. 10, it is clear that the location of the vortex cores are consistent throughout and the vortex strength and definition increases with increasing grid resolution. This better definition of the vortex is due to the decreased dissipation in the numerical scheme.

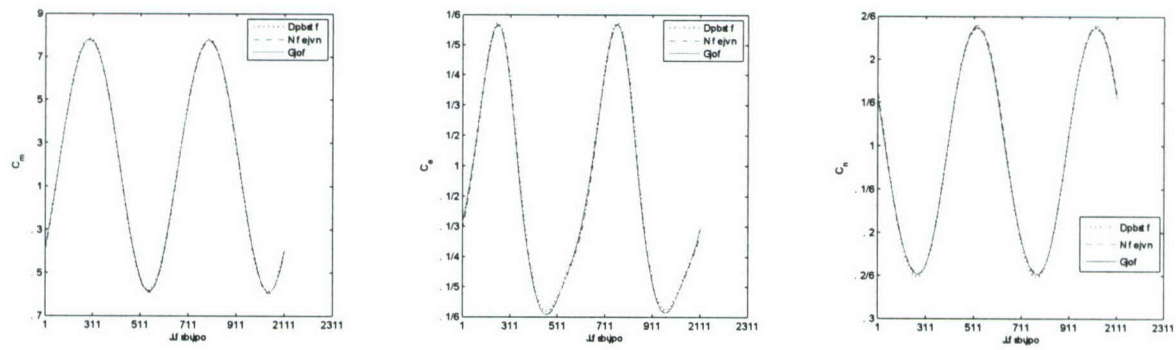

(a) C_l

(b) C_d

(c) $C_{m_{c/4}}$

Figure 9: Grid convergence of loads for pure-plunging case.

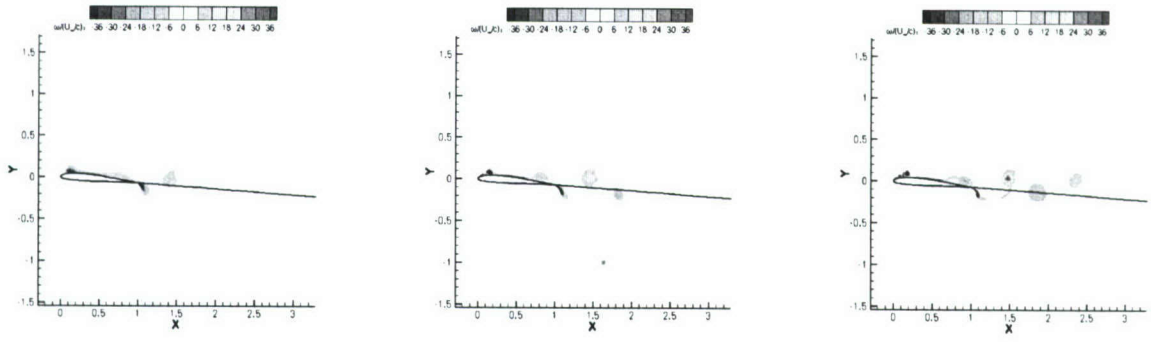

(a) Coarse (b) Medium (c) Fine

Figure 10: Vorticity contours for various grid sizes at the instant the airfoil is at the top of the plunging motion.

Load histories for the pure-pitching airfoil case are given in Figs. 11 (a)–(c). Although the trends, i.e., the overall shape of the curves, are being captured well, there is a substantial difference between the maximum values of each of the loads. This indicates a lack of grid convergence, especially when examining load values.

Examining Fig. 12, it is noted that the convergence of the wake region for the pure-pitch case is similar to that of the pure-plunge case, indicating that the grid resolution is critical in predicting the vorticity strength, particularly through the wake region. Examining Fig. 12, it is evident that the locations of the vortex cores are consistent throughout and the vortex strength and definition increases with increasing grid resultion.

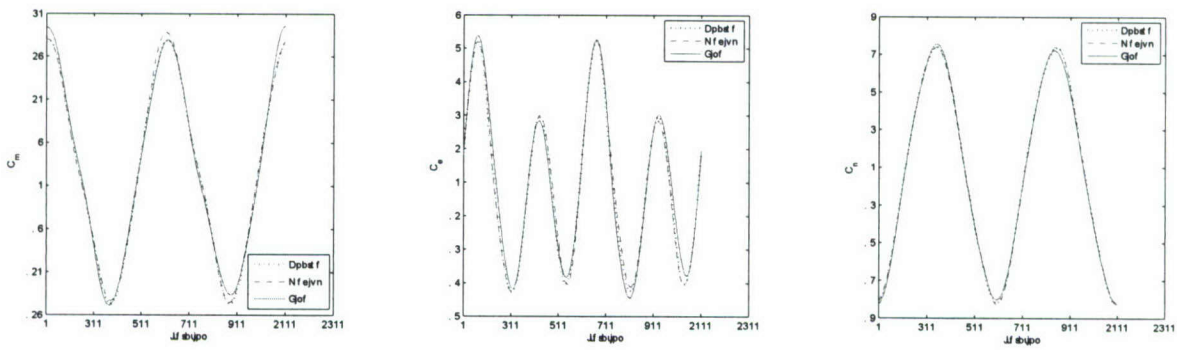

(a) C_l (b) C_d (c) $C_{m_{c/4}}$

Figure 11: Grid convergence of loads for pure-pitching case.

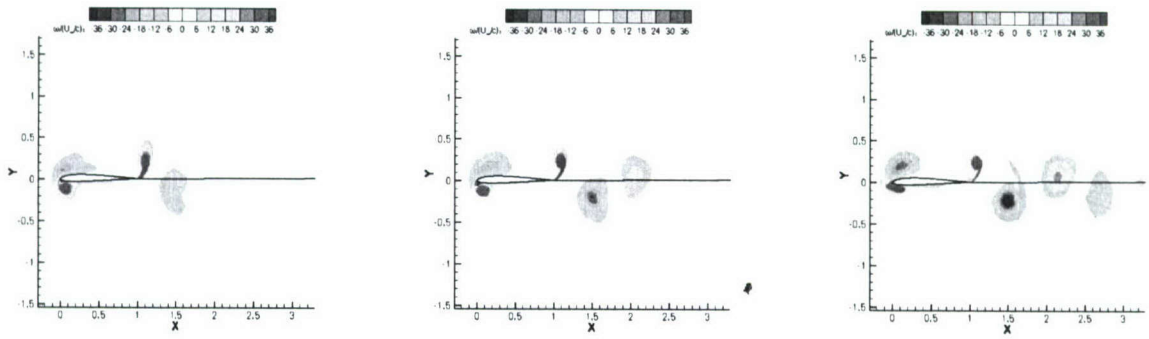

(a) Coarse (b) Medium (c) Fine

Figure 12: Vorticity contours for various grid sizes at the instant the airfoil is at the midpoint of the upward (increasing angle of attack) pitching motion.

Owing to this lack of convergence for the pitch case, a second grid, Fig. 13, was examined, this time with a denser spacing in the normal direction. The grid dimensions for the second grid were 689×257 for the fine, 345×129 for the medium, and 173×65 for the coarse. Load histories are shown in Fig. 14 and the vorticity contours for each grid level are given in Fig. 15. Again, similar to the findings of the coarser grid, for the pitch case the grid refinement impacts solely the strength and definition of each vortex core. The conclusion here is that, to reduce calculation time, it is sufficient to examine the finest level of the coarser grid, 689×113, for a qualitative comparison of the wake shapes to experiment.

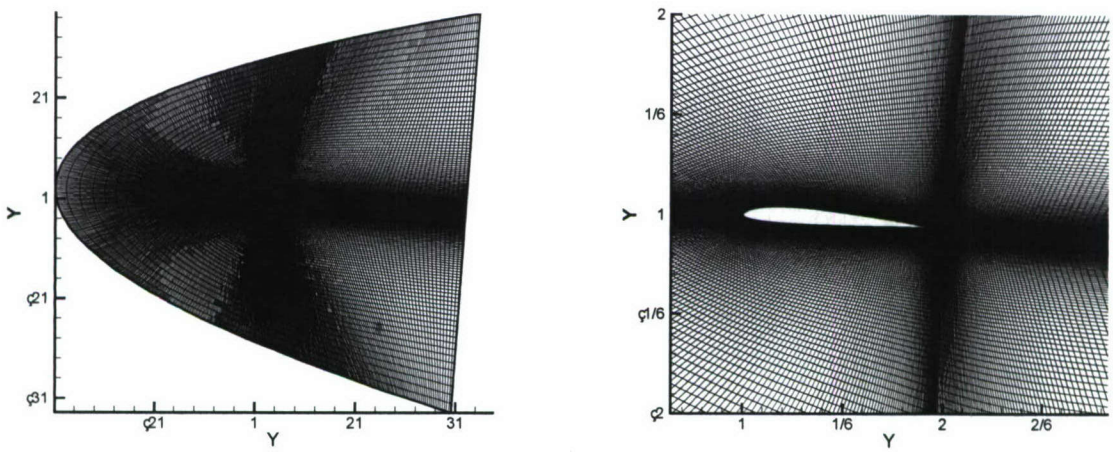

(a) Entire grid (b) Close up

Figure 13: Finer normal spacing grid utilized for grid convergence study of the pure-pitching case.

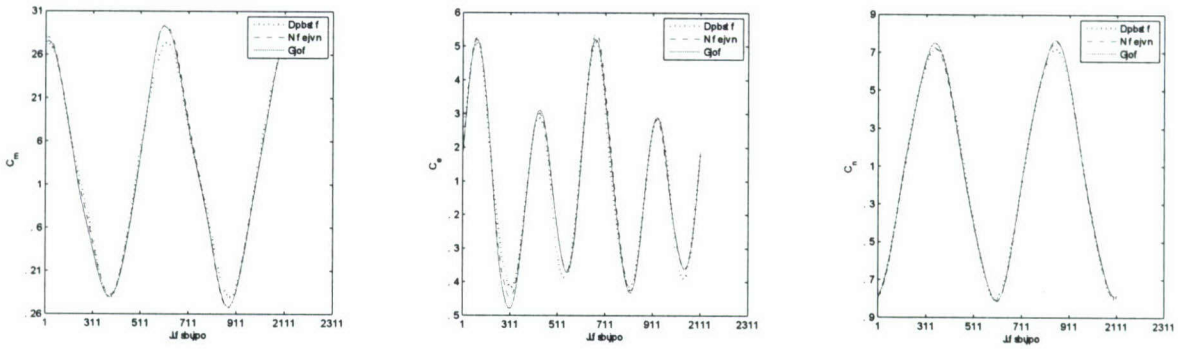

(a) C_l (b) C_d (c) $C_{m_{c/4}}$

Figure 14: Grid convergence of loads for pure-pitching case.

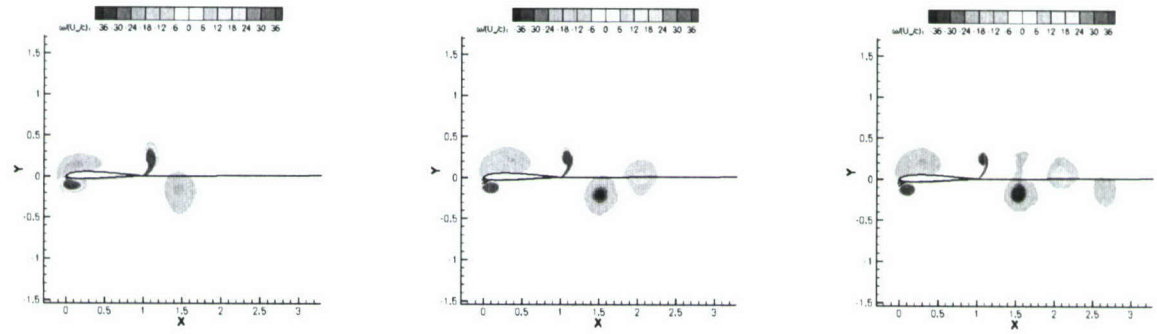

(a) Coarse (b) Medium (c) Fine

Figure 15: Vorticity contours for various grid sizes at the instant the airfoil is at the midpoint of the upward (increasing angle of attack) pitching motion.

3.4.2 Pure-Plunge at Re=40,000

Figure 16 gives a comparison of the non-dimensional streamwise velocity, u/U_∞. PIV results are in the leftmost column, CFL3D in the middle column, and NCSU immersed boundary method results in the rightmost column. Each row of figures corresponds to the phase, ϕ, at which the data was taken, i.e. beginning of cycle, $\frac{1}{4}$ of cycle, mid cycle, and $\frac{3}{4}$ of cycle, respectively. In the PIV there is a mask blanking the shadow of the laser light sheet. Overall the qualitative agreement amongst all three data sets is excellent. There are subtle differences in the velocity magnitudes, especially in the regions across the airfoils upper surface. Both CFD results accurately capture the strong shear layer that develops near the trailing edge during the plunge motion.

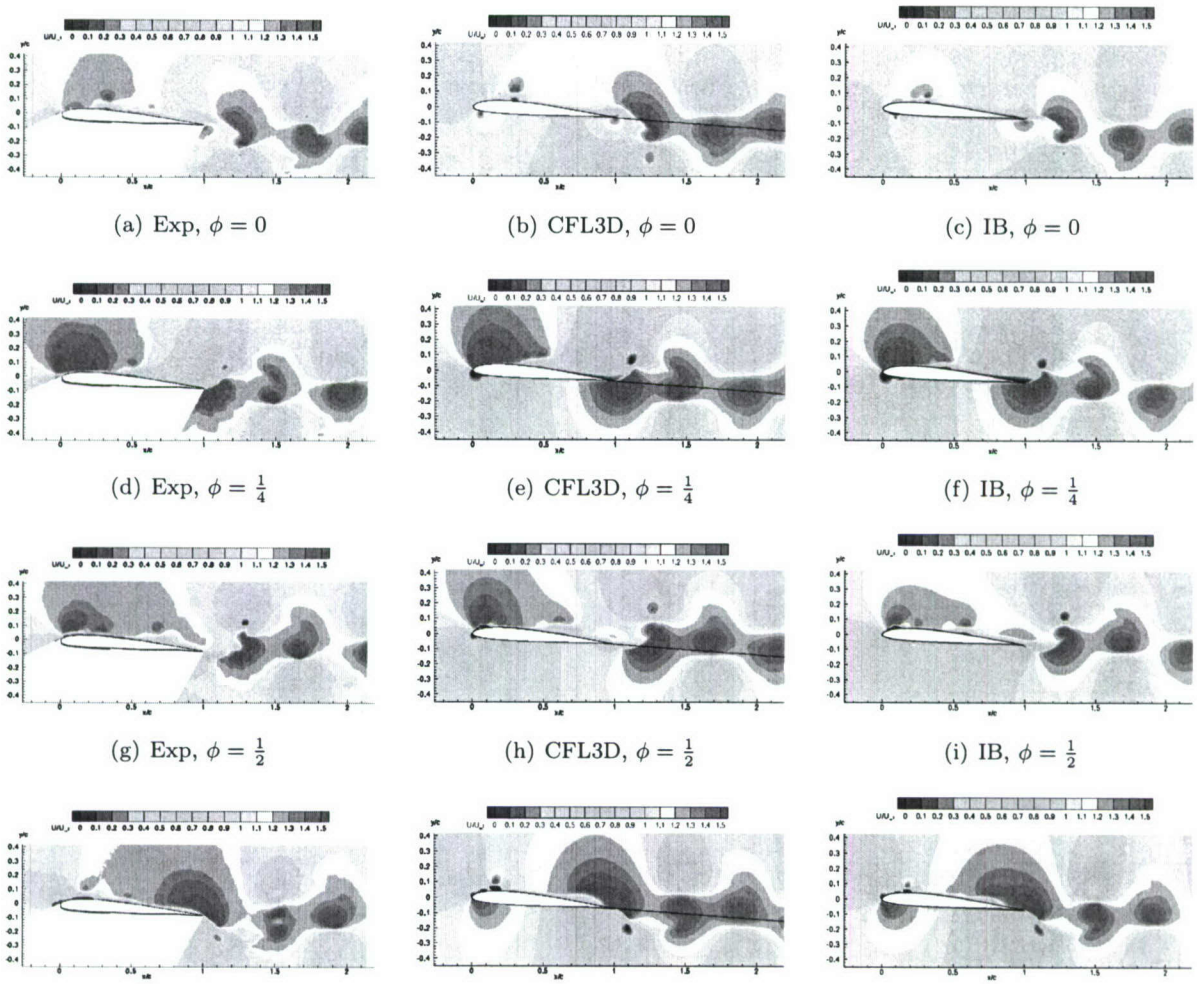

(a) Exp, $\phi = 0$ (b) CFL3D, $\phi = 0$ (c) IB, $\phi = 0$

(d) Exp, $\phi = \frac{1}{4}$ (e) CFL3D, $\phi = \frac{1}{4}$ (f) IB, $\phi = \frac{1}{4}$

(g) Exp, $\phi = \frac{1}{2}$ (h) CFL3D, $\phi = \frac{1}{2}$ (i) IB, $\phi = \frac{1}{2}$

(j) Exp, $\phi = \frac{3}{4}$ (k) CFL3D, $\phi = \frac{3}{4}$ (l) IB, $\phi = \frac{3}{4}$

Figure 16: Comparison of streamwise velocity contours from experiment, CFL3D, and immersed boundary method at various phases of motion; Re=40,000, pure-plunge.

Vorticity contours were examined to determine how accurately CFD was capturing the location of the shed vortex cores, with the working assumption of periodicity (necessary to justify phase averaging) of vortex shedding. Vorticity was normalized by airfoil chord and freestream velocity, with the near-zero levels blanked off for clarity. The plots of vorticity in Fig. 17 show that both CFD methods accurately match experiment in vortex core locations, but both also evince a dissipation that reduces vorticity peak magnitude in going downstream. Neither CFD method accurately captures the "fingering" of vorticity (shear layer rolls up into sequence of small discrete vortices) immediately downstream of the trailing edge. This is most prominent at $\phi = \frac{1}{4}$, where the effective angle of attack is maximum. The PIV, on the other hand, does not show as sharp a vorticity concentration for wall-bounded structures near the airfoil suction side. This could, however, be an effect of the phase-averaging process, in which minor variation period-to-period of vortex position tends to diminish apparent coherence when passing to the average. The PIV also shows a trail of negative vorticity upstream of the leading edge. This may be spurious, resulting from parallax effects in the camera view in the plane of the light sheet being partially blocked by the curvature of the leading edge.

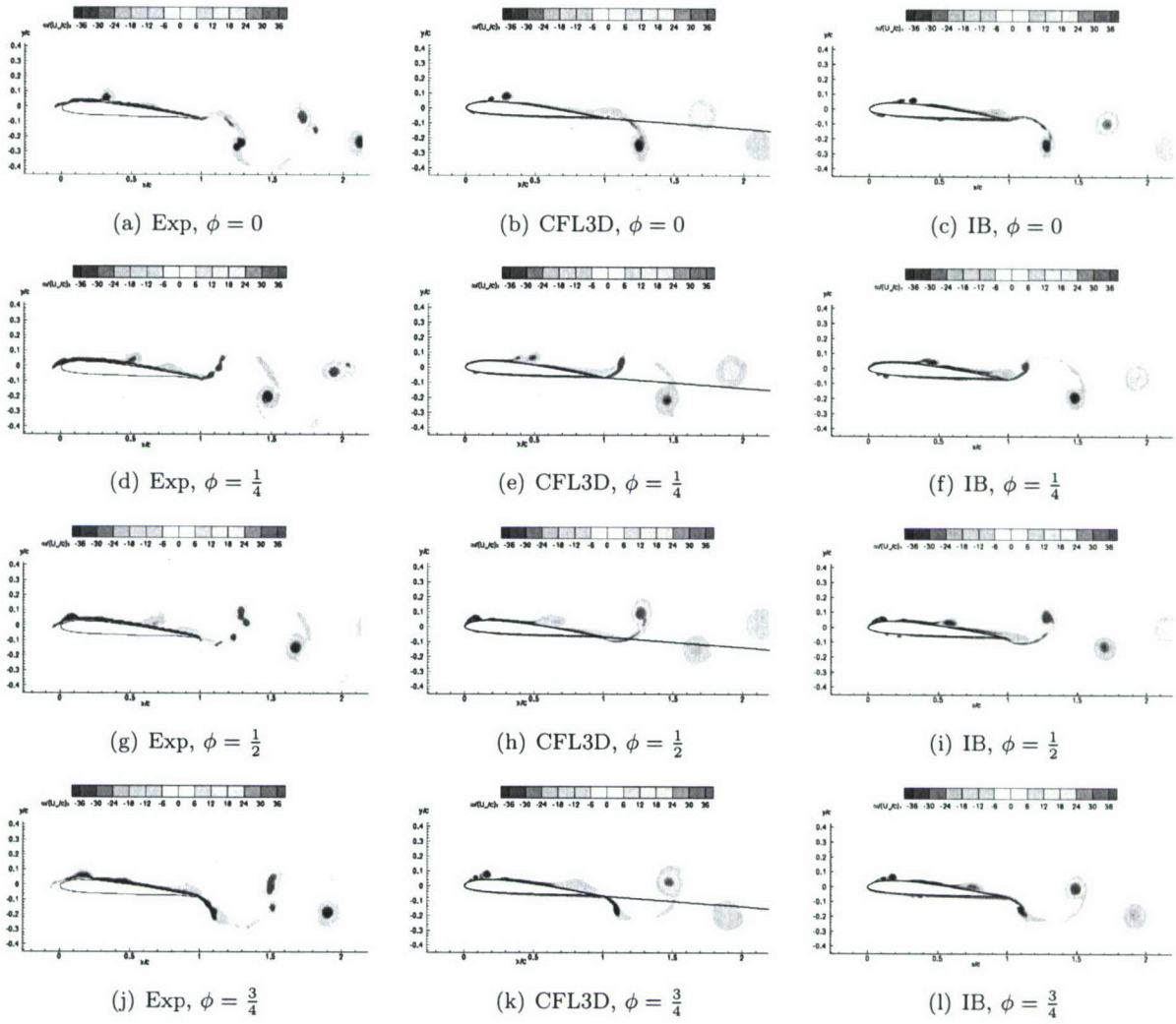

(a) Exp, $\phi = 0$ (b) CFL3D, $\phi = 0$ (c) IB, $\phi = 0$

(d) Exp, $\phi = \frac{1}{4}$ (e) CFL3D, $\phi = \frac{1}{4}$ (f) IB, $\phi = \frac{1}{4}$

(g) Exp, $\phi = \frac{1}{2}$ (h) CFL3D, $\phi = \frac{1}{2}$ (i) IB, $\phi = \frac{1}{2}$

(j) Exp, $\phi = \frac{3}{4}$ (k) CFL3D, $\phi = \frac{3}{4}$ (l) IB, $\phi = \frac{3}{4}$

Figure 17: Comparison of vorticity contours from experiment, CFL3D, and immersed boundary method at various phases of motion; Re=40,000, pure-plunge.

Figure 18 gives a comparison of the streamwise velocities in the wake at an x/c location of 2, or one chord length behind the airfoil. There is a good agreement between each of these with the exception of the mid-plunge location, $\phi = \frac{1}{2}$, Fig. 18 (c), where there is an extra "peak and valley" in the experimental velocity at $y/c = -0.3$. Furthermore, the magnitude of the peaks differ significantly at the $\phi = \frac{1}{4}$ location, Fig. 18 (b). The best agreement is when the phase is at $\frac{3}{4}$, Fig. 18 (d). Although there is currently no load data for comparison to experiment it can be deduced from Fig. 18 that, at least, the drag/thrust would compare well for these phases of motion.

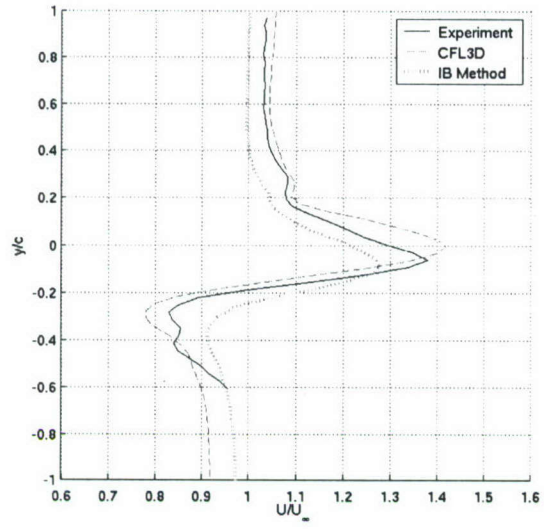

(a) $\phi = 0$

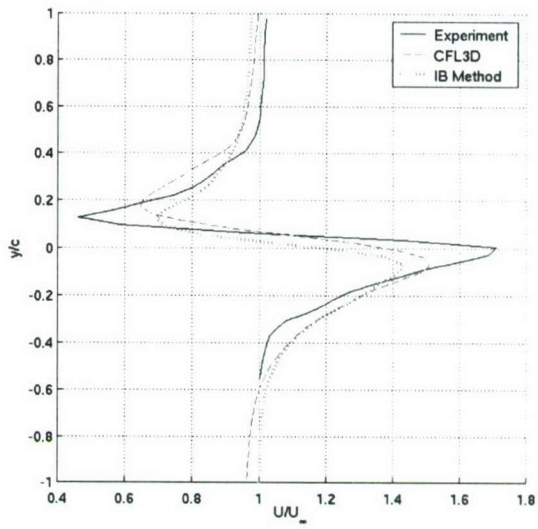

(b) $\phi = \frac{1}{4}$

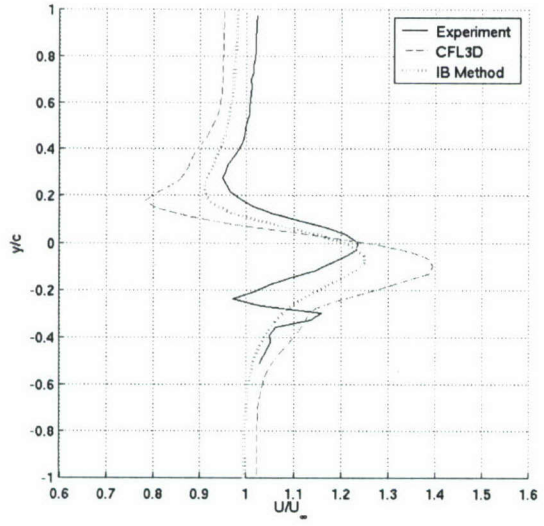

(c) $\phi = \frac{1}{2}$

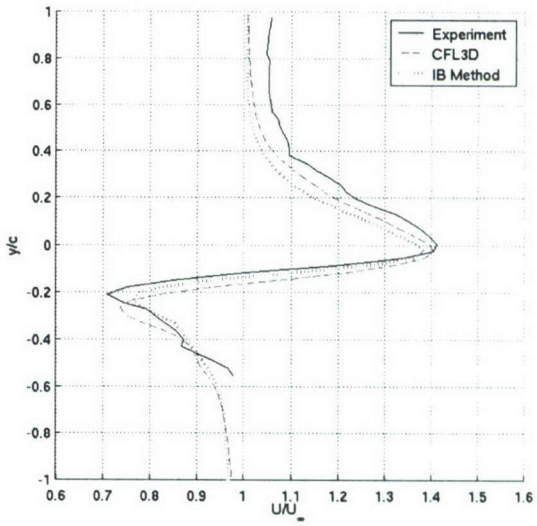

(d) $\phi = \frac{3}{4}$

Figure 18: Downstream wake profile comparisons; Re=40,000, $\frac{x}{c} = 2$, pure-plunge.

3.4.3 Pure-Pitch results at Re=40,000

In this section the results for the pitching case at $Re = 40,000$ is discussed. The figures follow the same format as those presented in Section 3.4.2. In an effort to assess blockage effects that may have been encountered in the experiment, the simulations were run with both CFL3D and immersed boundary method with the walls placed at $y/c = \pm 2$. The CFL3D simulation was also run without walls to determine how important it is to actually model them. Results shown in Fig. 19 indicate

that the absolute value of streamwise velocities in the experiment is much higher than those in both the CFD methods. Between the two CFD methods, the immersed boundary method predicts higher streamwise velocities than the CFL3D. These higher velocities are also manifested in the movement of the wake vortex cores, Fig. 20, as the wake vortex cores move downstream much quicker in the experiment. Another interesting observation is the upward movement of the vortex cores in the experiment. This type of structure has been observed in previous research with plunging airfoils at large Strouhal numbers.[13,25,26] In Ref. 13 the authors examine the wake structures for a range of nondimensional plunge velocities, kh. They indicate that for plunging airfoils with kh larger than 1 the upward motion, dubbed dual-mode, of the wake is present. Basing h on the distance traversed by the airfoil trailing-edge in pitch the kh for the SD7003 airfoil is 1.08. Therefore it is not surprising to see this type of structure present for the current pure-pitch experimental investigation. It is, however, surprising that neither of the CFD methods capture this behavior. Jones et al.[26] detail the sensitivity of this dual-mode behavior in both experiment and potential flow calculations using an unsteady panel method. The authors reveal that this behavior, with respect to experiments, is very sensitive to fluctuations in the flow as they observed the mode change during runs. The authors also indicate that the potential calculations, similar to the CFD methods presented here, did not capture the dual-mode behavior. They were, however, able to reproduce the behavior through very small timesteps in calculations.

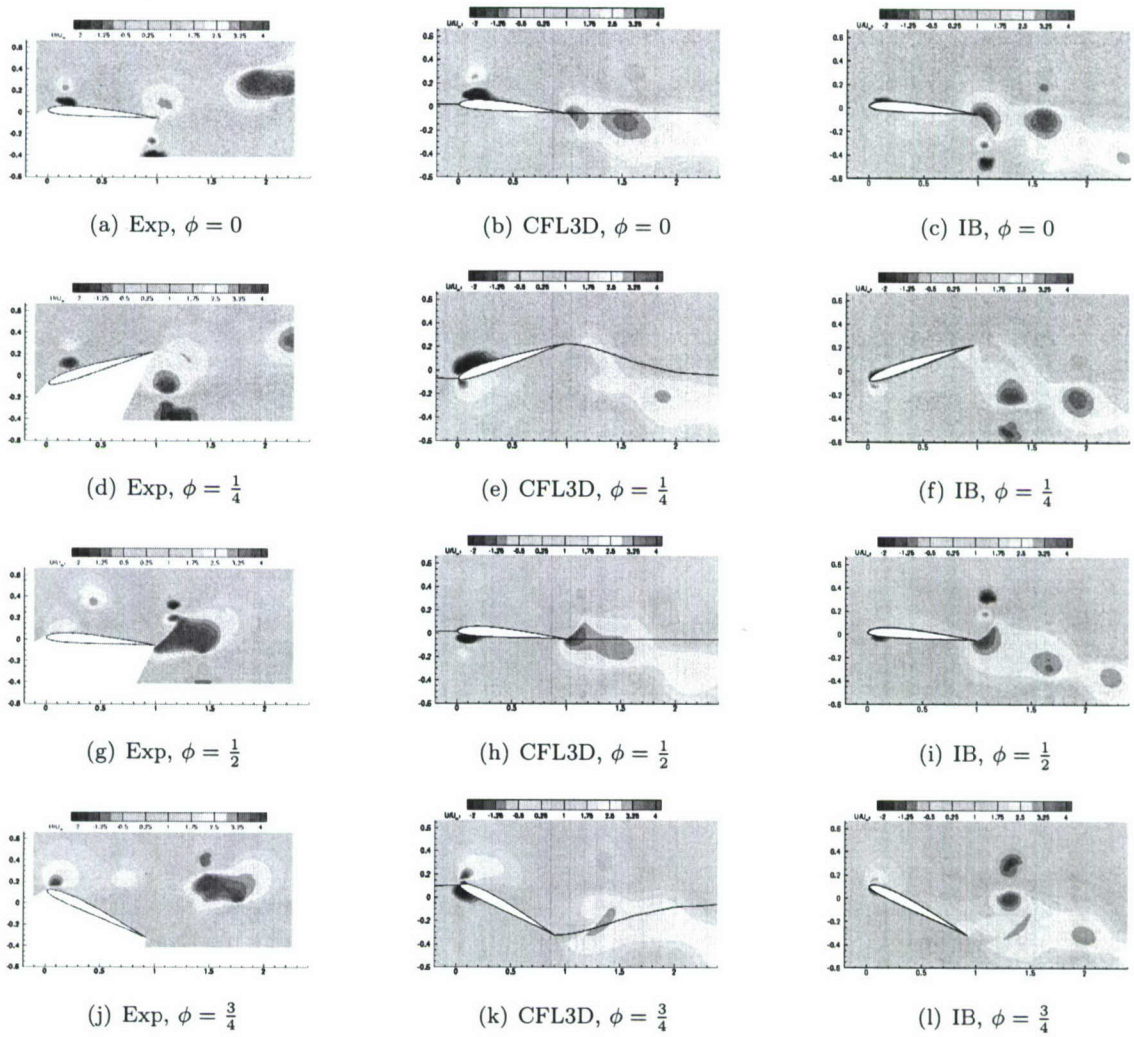

(a) Exp, $\phi = 0$ (b) CFL3D, $\phi = 0$ (c) IB, $\phi = 0$

(d) Exp, $\phi = \frac{1}{4}$ (e) CFL3D, $\phi = \frac{1}{4}$ (f) IB, $\phi = \frac{1}{4}$

(g) Exp, $\phi = \frac{1}{2}$ (h) CFL3D, $\phi = \frac{1}{2}$ (i) IB, $\phi = \frac{1}{2}$

(j) Exp, $\phi = \frac{3}{4}$ (k) CFL3D, $\phi = \frac{3}{4}$ (l) IB, $\phi = \frac{3}{4}$

Figure 19: Comparison of streamwise velocity contours from experiment, CFL3D with walls, and immersed boundary method with walls at various phases of motion; Re=40,000, pure-pitch.

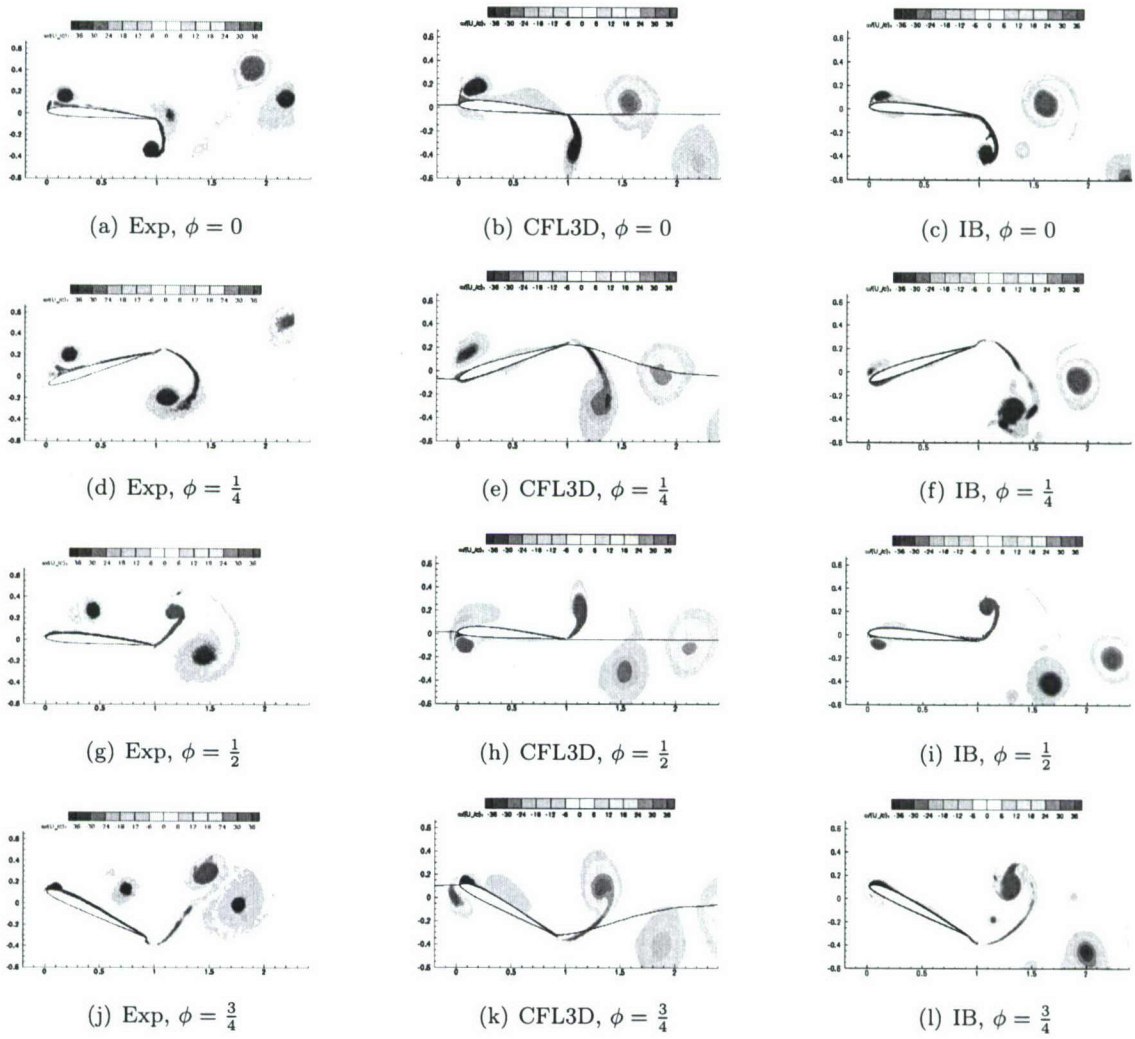

(a) Exp, $\phi = 0$ (b) CFL3D, $\phi = 0$ (c) IB, $\phi = 0$

(d) Exp, $\phi = \frac{1}{4}$ (e) CFL3D, $\phi = \frac{1}{4}$ (f) IB, $\phi = \frac{1}{4}$

(g) Exp, $\phi = \frac{1}{2}$ (h) CFL3D, $\phi = \frac{1}{2}$ (i) IB, $\phi = \frac{1}{2}$

(j) Exp, $\phi = \frac{3}{4}$ (k) CFL3D, $\phi = \frac{3}{4}$ (l) IB, $\phi = \frac{3}{4}$

Figure 20: Comparison of vorticity contours from experiment, CFL3D with walls, and immersed boundary method with walls at various phases of motion; Re=40,000, pure-pitch.

Figure 21 illustrates the effects that inclusion of walls has on the CFL3D simulation. Figures in the leftmost column represent the solution without walls; computational domain extends radially approximately 20 chord lengths from the airfoil as shown in Fig. 7. The figures in the rightmost column represent the computation with the presence of tunnel walls; computational grid for this configuration was shown in Fig. 8. From a qualitative stand point the walls have very little influence on the final CFL3D solution. It is, however, clear that with the presence of walls the vortices are weaker for all phases of motion.

Wake profiles shown in Fig. 22 also illustrate the differences between experiment and the two CFD methods for this pure-pitch case. Not only do the quantities from CFD differ from the experiment, but the CFD methods differ substantially from one another. Wake profiles from CFL3D with and without walls are nearly the same, indicating that it is a good assumption to ignore blockage effects. The dual-mode behavior that is present in the experiment is also discernible in the wake profiles.

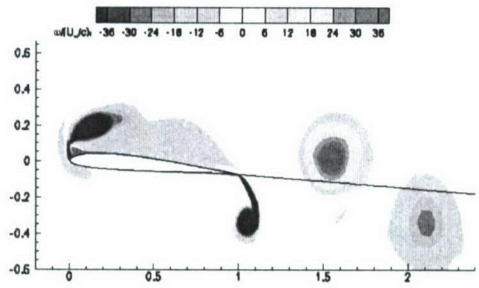

(a) CFL3D, $\phi = 0$

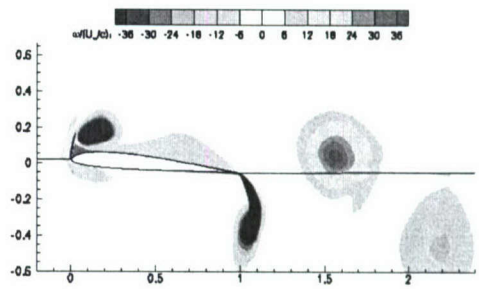

(b) CFL3D with walls, $\phi = 0$

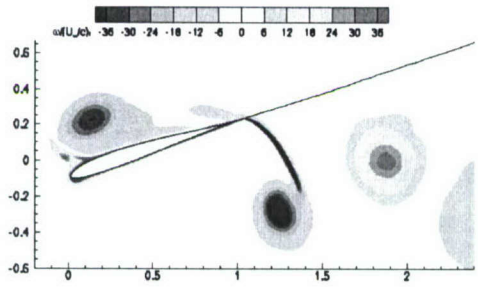

(c) CFL3D, $\phi = \frac{1}{4}$

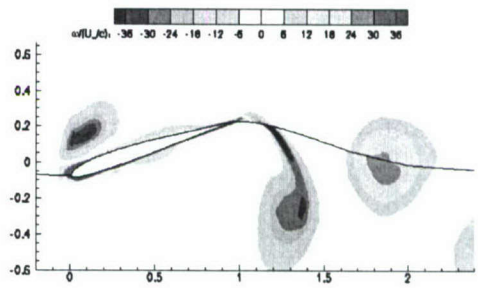

(d) CFL3D with walls, $\phi = \frac{1}{4}$

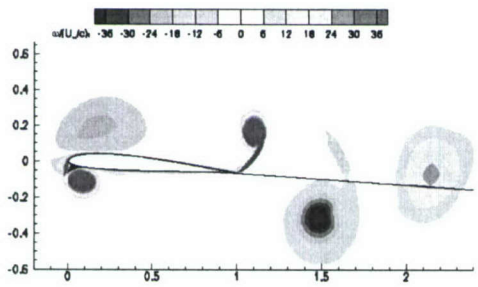

(e) CFL3D, $\phi = \frac{1}{2}$

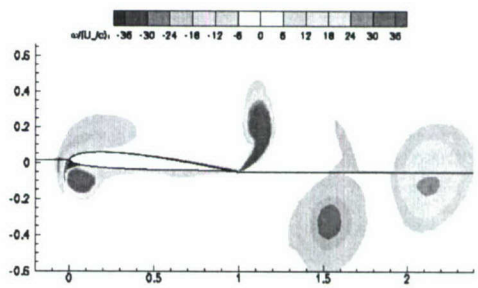

(f) CFL3D with walls, $\phi = \frac{1}{2}$

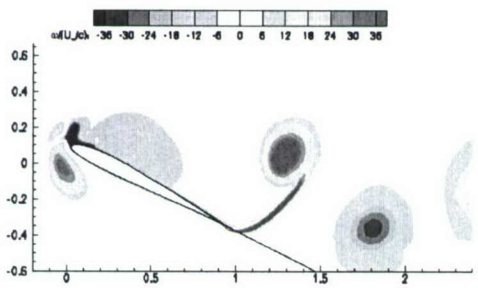

(g) CFL3D, $\phi = \frac{3}{4}$

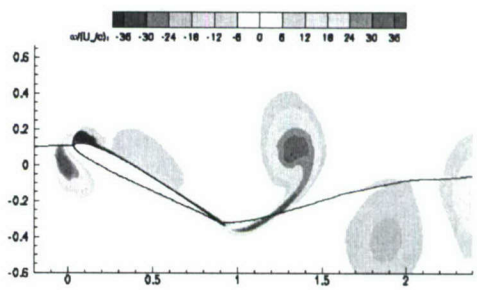

(h) CFL3D with walls, $\phi = \frac{3}{4}$

Figure 21: Wall effects on vorticity contours from CFL3D solutions; Re=40,000, pure-pitch.

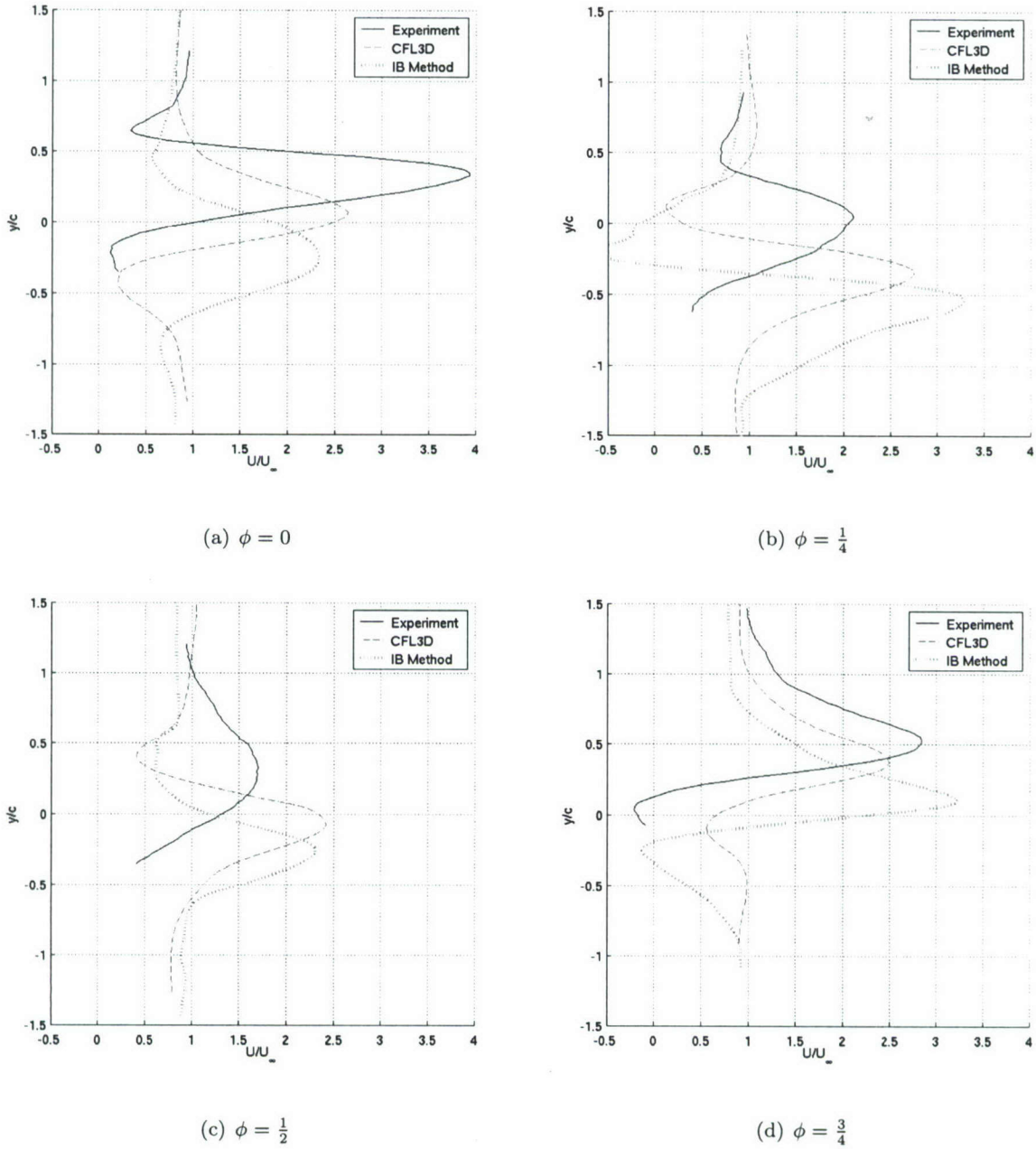

(a) $\phi = 0$

(b) $\phi = \frac{1}{4}$

(c) $\phi = \frac{1}{2}$

(d) $\phi = \frac{3}{4}$

Figure 22: Downstream wake profile comparisons; Re=40,000, $\frac{x}{c} = 2$, pure-pitch.

3.4.4 Pure-Plunge at Re=10,000

In this section the effects of Reynolds number on the plunging case is examined in detail. Immersed boundary computational results for the $Re = 10,000$ cases are omitted. For the results from the $Re = 40,000$ plunge case, the reader is referred to Section 3.4.2. As with the $Re = 40,000$ cases, the experiment and computation agree well here. The streamwise velocity, Fig. 23, shows a good qualitative agreement. The similarities at very different Reynolds numbers are a good indication

that the issues with calculating stability/transition are not inherently important here. Comparing Fig. 23 with Fig. 16 it is noted that, for this magnitude of change, the Reynolds number has a negligible influence on both the experiments and CFD solution. Vorticity contours, shown in Fig. 24, also compare very well between CFD and experiment. Comparing Fig. 24 to Fig. 17 again very little difference is seen between the two Reynolds numbers. The fingering effect of the vorticity in the experiments discussed in Section 3.4.2 is not as prominent at the lower Re. Figure 25 shows good agreement in wake profiles between CFD and experiment at $Re = 10,000$. Comparing to Fig. 18 it is observed that while CFD results are affected very little, the experiment has a much more rounded peaks in vorticity through the wake for the $Re = 10,000$ case.

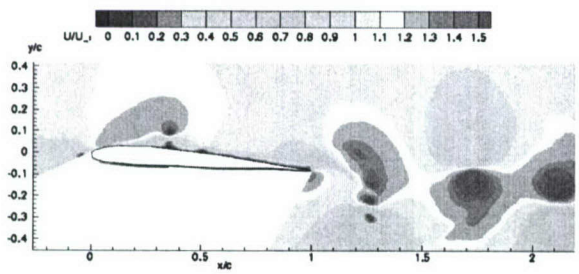

(a) Exp, $\phi = 0$

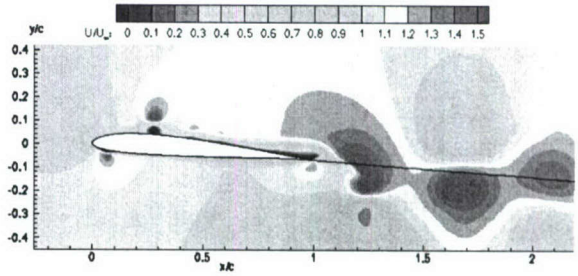

(b) CFL3D, $\phi = 0$

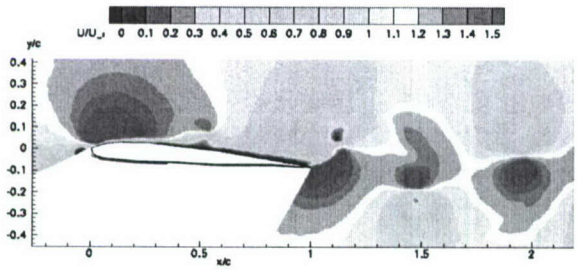

(c) Exp, $\phi = \frac{1}{4}$

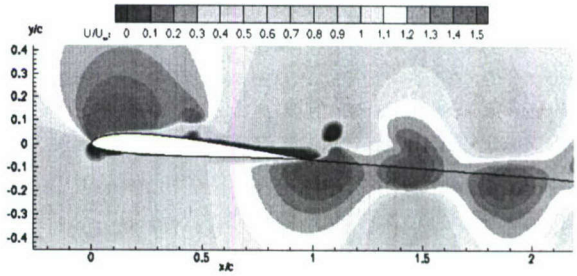

(d) CFL3D, $\phi = \frac{1}{4}$

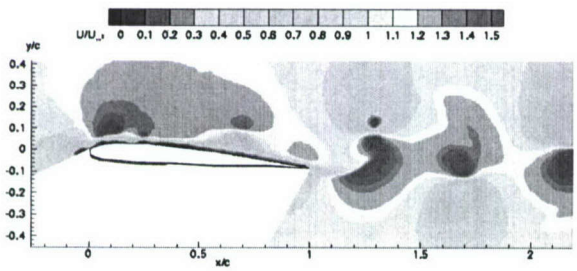

(e) Exp, $\phi = \frac{1}{2}$

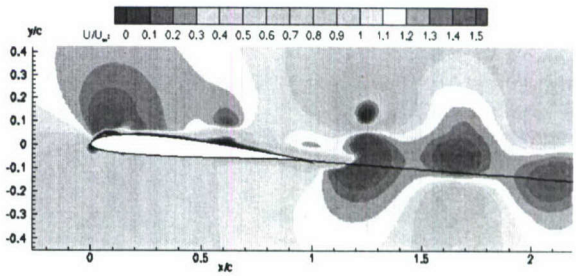

(f) CFL3D, $\phi = \frac{1}{2}$

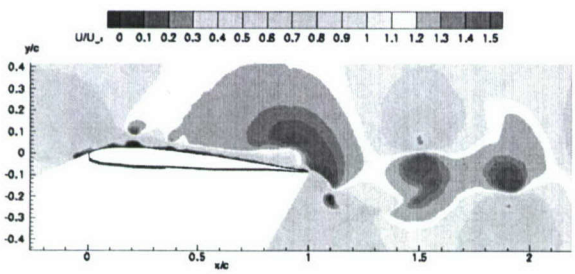

(g) Exp, $\phi = \frac{3}{4}$

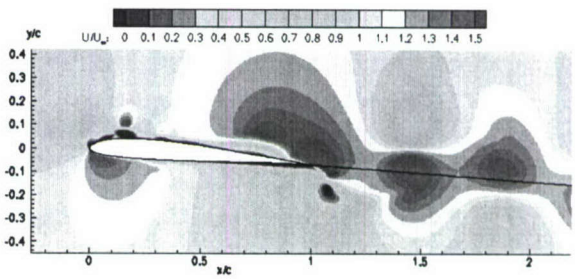

(h) CFL3D, $\phi = \frac{3}{4}$

Figure 23: Comparison of streamwise velocity contours from experiment and CFL3D for $Re = 10,000$, pure-plunge.

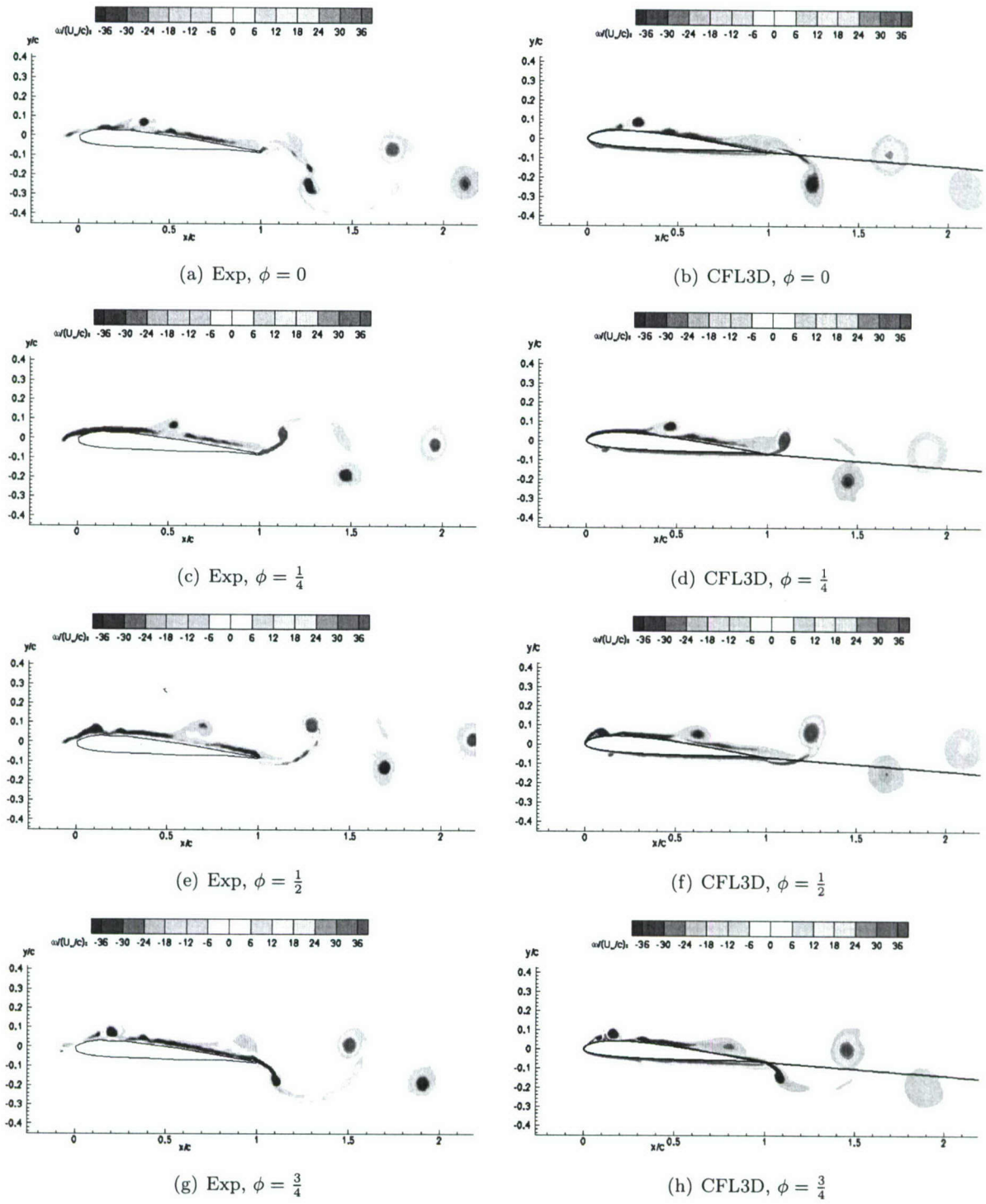

(a) Exp, $\phi = 0$

(b) CFL3D, $\phi = 0$

(c) Exp, $\phi = \frac{1}{4}$

(d) CFL3D, $\phi = \frac{1}{4}$

(e) Exp, $\phi = \frac{1}{2}$

(f) CFL3D, $\phi = \frac{1}{2}$

(g) Exp, $\phi = \frac{3}{4}$

(h) CFL3D, $\phi = \frac{3}{4}$

Figure 24: Comparison of vorticity contours from experiment and CFL3D for $Re = 10,000$, pure-plunge.

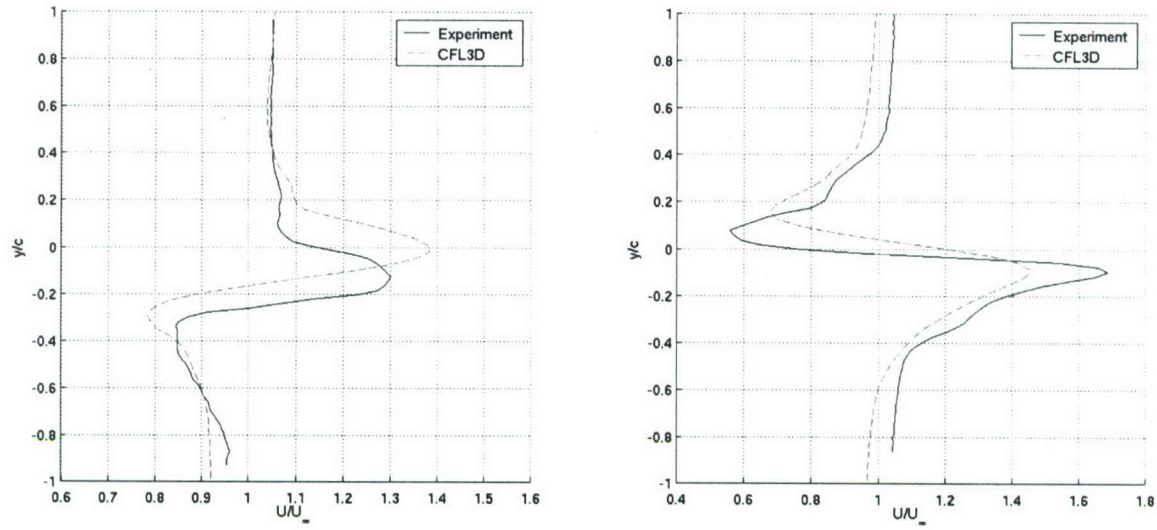

(a) $\phi = 0$

(b) $\phi = \frac{1}{4}$

(c) $\phi = \frac{1}{2}$

(d) $\phi = \frac{3}{4}$

Figure 25: Downstream wake profile comparisons between Experiment and CFL3D; $Re = 10,000$, $\frac{x}{c} = 2$, pure-plunge.

3.4.5 Pure-Pitch at Re=10,000

Here the results for pure-pitch at $Re = 10,000$ are examined. Figure 26, similar to the $Re = 40,000$ case, shows that for pitching the CFD again compares poorly with experiments, missing both velocity magnitude and concentration locations. Comparing with Fig. 19 there is very little respective difference between $Re = 40,000$ and $Re = 10,000$ for either the experiment or the

numerics. Vorticity contours presented in Fig. 27 show that the presence of the dual-mode behavior of the wake is still present at this Reynolds number. Here too, as in the $Re = 40,000$ case, the computation fails to predict this behavior. Comparing the experimental results in Fig. 27 to those in Fig. 20, it is interesting to note that the fingering effect, mentioned in Section 3.4.2, has the opposite behavior in pitch as in plunge. For this pitching case the fingering is more evident at the lower Reynolds number, where as for plunging it was more evident at the higher Reynolds number. Wake profiles shown in Fig. 28 compare well with the corresponding profiles from the higher Reynolds number case in Fig. 22, again indicating the lack of a Reynolds number effect.

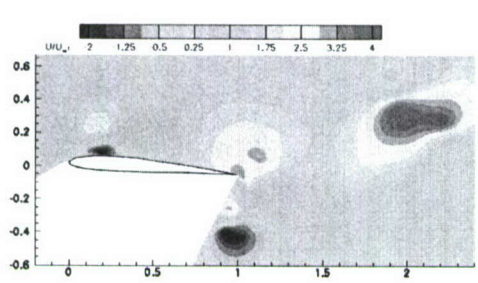

(a) Exp, $\phi = 0$

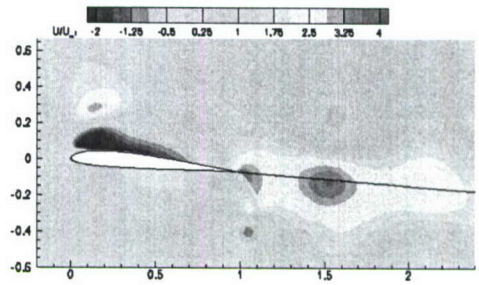

(b) CFL3D, $\phi = 0$

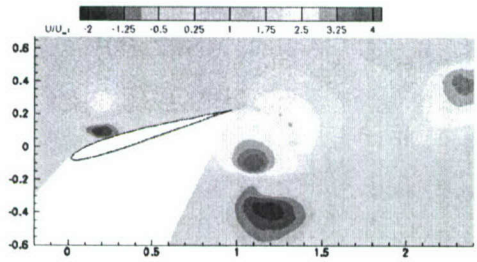

(c) Exp, $\phi = \frac{1}{4}$

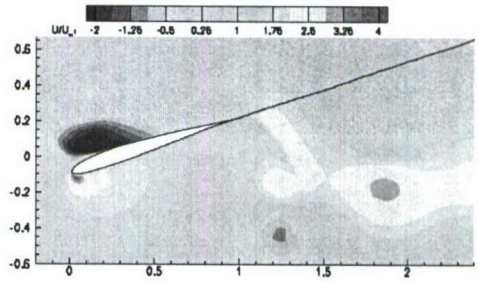

(d) CFL3D, $\phi = \frac{1}{4}$

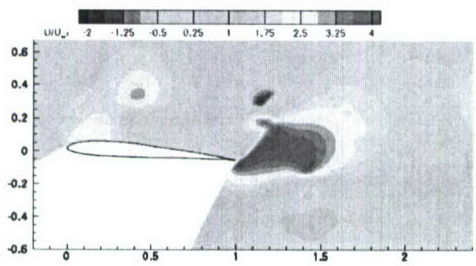

(e) Exp, $\phi = \frac{1}{2}$

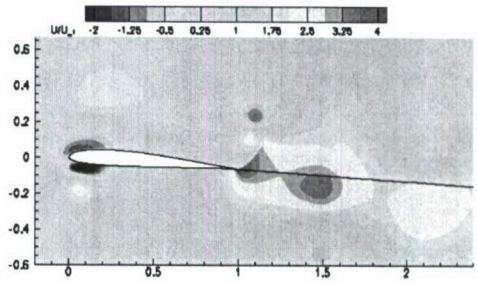

(f) CFL3D, $\phi = \frac{1}{2}$

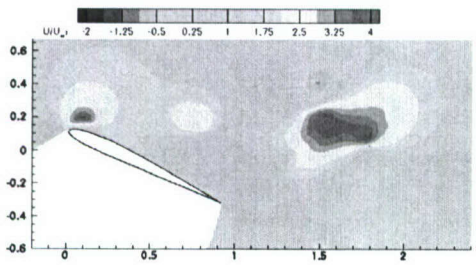

(g) Exp, $\phi = \frac{3}{4}$

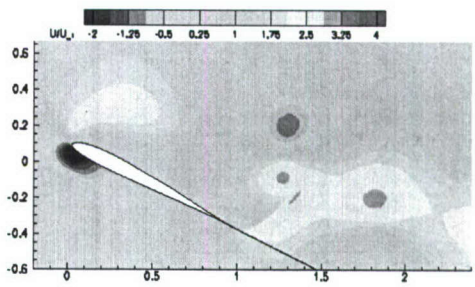

(h) CFL3D, $\phi = \frac{3}{4}$

Figure 26: Comparison of streamwise velocity contours from experiment and CFL3D for $Re = 10,000$, pure-pitch.

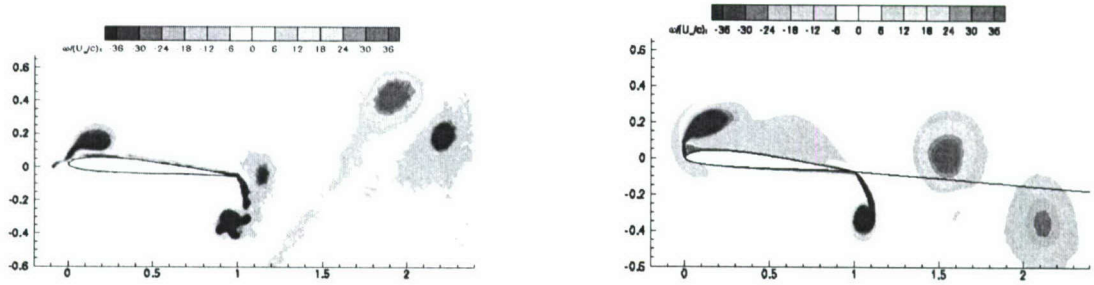

(a) Exp, $\phi = 0$

(b) CFL3D, $\phi = 0$

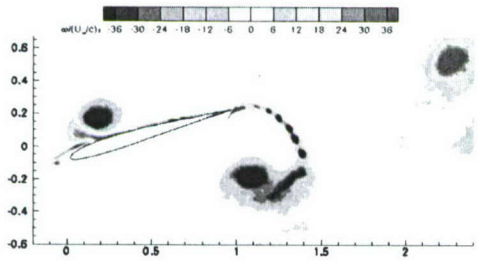

(c) Exp, $\phi = \frac{1}{4}$

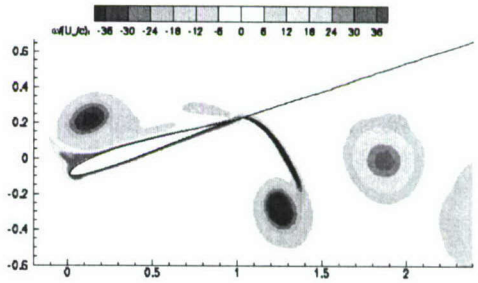

(d) CFL3D, $\phi = \frac{1}{4}$

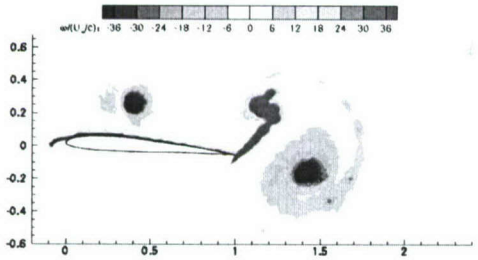

(e) Exp, $\phi = \frac{1}{2}$

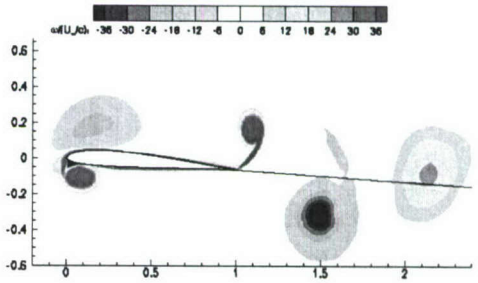

(f) CFL3D, $\phi = \frac{1}{2}$

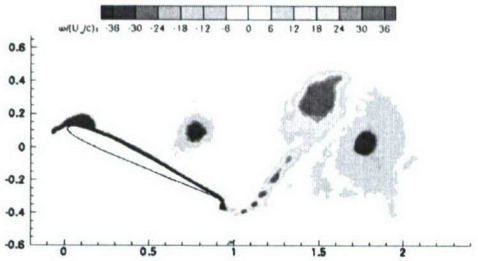

(g) Exp, $\phi = \frac{3}{4}$

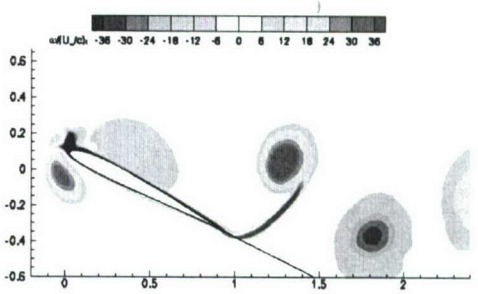

(h) CFL3D, $\phi = \frac{3}{4}$

Figure 27: Comparison of vorticity contours from experiment and CFL3D for $Re = 10,000$, pure-pitch.

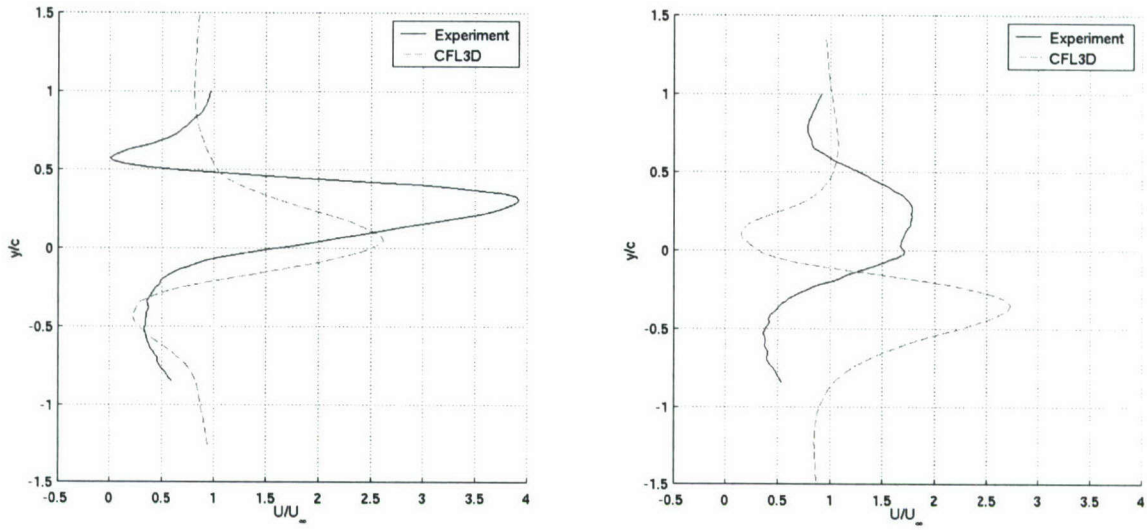

(a) $\phi = 0$

(b) $\phi = \frac{1}{4}$

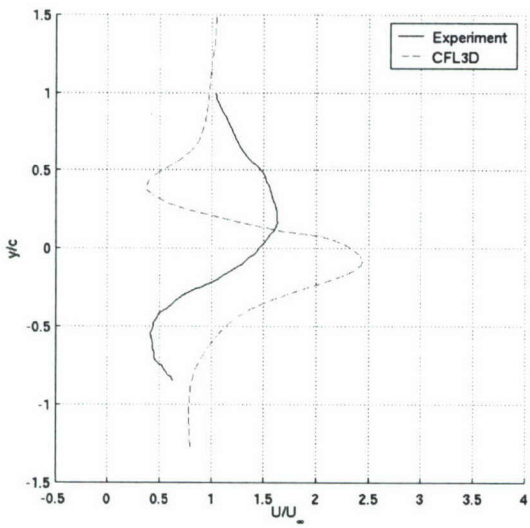

(c) $\phi = \frac{1}{2}$

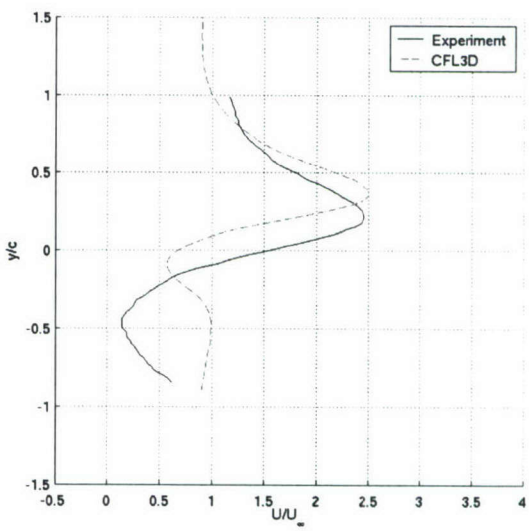

(d) $\phi = \frac{3}{4}$

Figure 28: Downstream wake profile comparisons between Experiment and CFL3D; $Re = 10,000$, $\frac{x}{c} = 2$, pure-pitch.

3.5 Phase 2 Summary

High-frequency ($k = 3.93$) pitching and plunging motions of the SD7003 airfoil were examined experimentally with particle image velocimetry, and computationally via two different codes. Reynolds number effects were considered by comparing the "high Re" case of 40,000, with the "low Re" case of 10,000. Comparisons were made between streamwise velocity contours (both as a field variable

and through the wake one chord downstream of the trailing edge) and vorticity.

For the pure-plunge case the computational methods, NASA's CFL3D research code and NCSU immersed boundary method, show good quantitative agreement to the experimental results. This agreement shows that the type of computational model is not very significant. Furthermore, it also suggests that the blockage and rigging effects in experiment are not substantial and that the experiment can be treated as two-dimensional. Somewhat surprisingly, the pure-pitching case shows very poor agreement. The inclusion of walls into the computation of the pure-pitching case showed that apparent blockage effects are negligible, and thus was not responsible for the disagreement with experiment. For all cases, experiment and CFD, the $Re = 40,000$ flow was very similar to the $Re = 10,000$ flow, implying little Reynolds number sensitivity for the high-frequency motions studied here.

The significant difference in experimental results between pure-plunge and pure-pitch raises basic questions on the validity of the definition of angle of attack used to construct the two motions, and also suggests nontrivial nonlinearities in flowfield response for a given angle of attack time history.

4 Phase 3

The effort comparing computation and experiment for high intensity pitch/plunge oscillations in Phase 2 (Sec. 3) brings to the attention two questions that need to be addressed. First, what is the cause of the discrepancy between experimental and computational results for the pure-pitching case? Second, is there a combination of parameters (reduced amplitude, pivot point, etc.)that will achieve equivalence between pitch and plunge motions?

For the first question there is a number of possible explanations. Perhaps the most obvious, and likely explanation, is the lack of three-dimensional effects in the computational results. It is likely that with such an aggressive pitch motion, the 3-D effects due to side wall interaction with tip vortices cannot be ignored. Another possibility lies in the "correct" modeling of the airfoil's trailing edge. In the current computations the airfoil is modeled with a sharp trailing edge. Although it is extremely thin on the actual airfoil model used in the experiments, the trailing edge does have a small thickness of approximately 0.2% of the chord. It has been shown in Ref. 27 that the treatment of the trailing edge in computations plays a crucial role in the final results.

With regards to the question of pitch-plunge equivalence, it is believed that, by suitable choice of parameters, it will be possible to generate a $C_l(t)$ with pure pitch that is similar to the $C_l(t)$ achieved with a pure-plunge oscillation.

4.1 On-Going Research

The intention in this on-going research is to utilize the analytical method of Theodorsen[28] in a effort to search for the parameters that would result in pitch-plunge equivalence. Utilizing Theodorsen's expression for lift, Eqn. 3, it is possible to separate the terms due to pure-pitching motions, Eqn. 4, from those due to pure-plunging, Eqn. 5. If there exists a combination of pitch amplitude, plunge amplitude, and rotation point where the $C_l(t)$ due to each motion are equivalent, then at that condition there will be an equivalence between the pitch and plunge motions.

$$C_l = \pi c \left(\frac{\dot{\alpha}}{U_\infty} + \frac{\ddot{h}}{U_\infty^2} - \frac{ca\ddot{\alpha}}{U_\infty^2} \right) - 2\pi C(k) \left[\frac{\dot{h}}{U_\infty} + \alpha + c\left(\frac{1}{2} - a\right) \frac{\dot{\alpha}}{U_\infty} \right] \tag{3}$$

$$C_{l_{pitch}} = \pi c \left(\frac{\dot{\alpha}}{U_\infty} - \frac{ca\ddot{\alpha}}{U_\infty^2} \right) - 2\pi C(k) \left[c\left(\frac{1}{2} - a\right) \frac{\dot{\alpha}}{U_\infty} \right] \tag{4}$$

$$C_{l_{plunge}} = \pi c \left(\frac{\ddot{h}}{U_\infty^2} \right) - 2\pi C(k) \left[\frac{\dot{h}}{U_\infty} \right] \tag{5}$$

Here, c is the chord length of the airfoil and a is the distance to the pivot point, x_{rot}, from the mid-chord point of the airfoil. The expression for a is given in Eqn. 6. The function $C(k)$ is the Theodorsen function given in Eqn. 7. Here, K_1 is the first-order Bessel function of the second kind and K_0 is the zeroth-order Bessel function of the second kind.

$$a = 2\frac{x_{rot}}{c} - 1 \tag{6}$$

$$C(k) = \frac{K_1(ik)}{K_1(ik) + K_0(ik)} \tag{7}$$

This will also be examined using the UnsTAT code discussed in Section 2.1. If the study points to pitch/plunge parameters that will result in equivalence, those motions will be examined both computationally and experimentally to validate the findings.

5 Conclusions and Future Directions

Starting with the development of low-order unsteady thin airfoil theory (UnsTAT) model, the focus of the effort shifted to comparison between higher-order computational methods (RANS) and experimental results for high-frequency pure-pitch and pure-plunge oscillations at low Reynolds numbers. The redirected effort brought to light two questions. First, what parameters will result in equivalence between pitch and plunge? Second, what is the reason for discrepancies between computation and experiment for the pure-pitch oscillation in Sec. 3? Answering both these questions is important for understanding the fundamentals of airfoils and wings undergoing unsteady motions.

Seeking the answer to the first question of pitch-plunge equivalence is likely to result in insight into the design of motions that can produce desired loads as a function of time. Such insight is necessary for the design of efficient micro air vehicles, for which wing motion and/or flexibility is almost unavoidable. The on-going work is focused on answering this questions, using analytical approaches as a first step. If successful, computational and experimental investigations will follow to gain further understanding. This on-going work is expected to lead to and be a part of Mr. McGowan's Ph.D. dissertation.

Seeking the answer to the second question is vital for the development of reliable computational tools and experimental methods for unsteady motions at low Reynolds numbers—another key requirement for successful development of future micro air vehicles. This question sets one of the future directions for the current research—to determine the reason for poor comparison between

computation and experiment for the pure-pitch oscillation described in Sec. 3. The reasons, as mentioned earlier, may lie in the three dimensionality of the flow fields for the high intensity of pitching oscillations used in the current research.

Another future direction is the determination of bounds within which low-order methods can be used reliably for flight dynamics modeling and control of micro air vehicles. For such purposes, high-order computational methods are not suitable because of their high computational cost. By using both low- and high-order computational methods in the study of unsteady motions of airfoils and wings at low Reynolds numbers, and by comparison with experiments, it is believed that such bounds for the low-order methods can be determined allowing for judicious use of such models for micro air vehicle design, modeling and control.

6 Acknowledgments

The authors wish to gratefully acknowledge the collaboration and support of Dr. Michael Ol of AFRL/VAAA and Prof. Jack Edwards of NCSU in this research and their significant contributions to the research presented in this report.

References

[1] Ol, M. V., "Vortical Structures in High Frequency Pitch and Plunge at Low Reynolds Number," AIAA Paper 2007–4233, June 2007.

[2] Krist, S. L., Biedron, R. T., and Rumsey, C. L., "CFL3D User's Manual," NASA TM 208444, 1998.

[3] McGowan, G. Z., Gopalarathnam, A., Ol, M. V., Edwards, J. R., and Fredberg, D., "Computation vs. Experiment for Hight-Frequency Low-Reynolds Number Airfoil Pitch and Plunge," AIAA Paper 2008–0653, January 2008.

[4] Katz, J. and Plotkin, A., *Low-Speed Aerodynamics From Wing Theory to Panel Methods*, McGraw-Hill, Inc., 1991.

[5] Young, J., *Numerical Simulation of the Unsteady Aerodynamics of Flapping Airfoils*, Ph.D. thesis, The University of New South Wales, Australia, May 2005.

[6] Fung, Y. C., *An Introduction to the Theory of Aeroelasticity*, John Wiley and Sons, New York, 1955.

[7] Basu, B. C. and Hancock, G. J., "The Unsteady Motion of a Two-Dimensional Aerofoil in Incompressible Inviscid Flow," *Journal of Fluid Mechanics*, Vol. 87, No. 1, 1978, pp. 159–178.

[8] Piziali, R. A., "An Experimental Investigation of 2D and 3D Oscillating Wing Aerodynamics for a Range of Angles of Attack Including Stall," NASA TM 4632, September 1993.

[9] von Kármán, T. and Sears, W., "Airfoil Theory for Non-Uniform Motion," *Journal of the Aeronautical Sciences*, Vol. 5, No. 10, August 1938, pp. 379–390.

[10] McCroskey, W. J., "The Phenomenon of Dynamic Stall," NASA TM 81264, 1981.

[11] Mueller, T. J., "Low Reynolds Number Vehicles," AGARDograph No. 288, 1985.

[12] Etkin, B., *Dynamics of Atmospheric Flight*, Dover Publications, 2000.

[13] Lai, J. C. S. and Platzer, M., "Jet Characteristics of a Plunging Airfoil," *AIAA Journal*, Vol. 37, No. 12, December 1999, pp. 1529–1537.

[14] *http://www.ae.uiuc.edu/m-selig/ads/coord_database.html.*

[15] Ol, M., McAuliffe, B., Hanff, E., Scholz, U., and Kähler, C., "Comparison of Laminar Separation Bubble Measurements on a Low Reynolds Number Airfoil in Three Facilities," AIAA Paper 2005–5149, June 2005.

[16] Leishman, J. G., *Principles of Helicopter Aerodynamics*, Cambridge Aerospace Series, 2002.

[17] Willert, C. E. and Gharib, M., "Digital Particle Image Velocimetry," *Experiments in Fluids*, 1991, pp. 181–193.

[18] Spalart, P. R. and Allmaras, S. R., "A One-Equation Turbulence Model for Aerodynamic Flows," AIAA Paper 92–0439, 1992.

[19] Edwards, J. R. and Thomas, J. L., "Development and Investigation of $O(Nm^2)$ Preconditioned Multigrid Solvers for the Euler and Navier-Stokes Equations," AIAA Paper 99–3263, 1999.

[20] Bartels, R. E., "Finite Macro-Element Mesh Deformation in a Structured Multi-Block Navier-Stokes Code," NASA TM 2005, 2005.

[21] Mohd-Yusof, J., "Development of Immersed Boundary Methods for Complex Geometries," *Center for Turbulence Research Annual Research Briefs*, 1998, pp. 325–336.

[22] Mohd-Yusof, J., "Combined Immersed Boundaries/B-splines Methods for Simulation of Flows in Compex Geometries," *Center for Turbulence Research Annual Research Briefs*, 1997, pp. 317–327.

[23] Peskin, C. S., "Flow Patterns Around Heart Valves: A Numerical Method," *Journal of Computational Physics*, Vol. 10, No. 2, October 1972, pp. 220–252.

[24] Choi, J.-I., Oberoi, R. C., Edwards, J. R., and Rosati, J. A., "An Immersed Boundary Method for Complex Incompressible Flows," *Journal of Computational Physics*, Vol. 224, No. 2, June 2007, pp. 757–784.

[25] Jones, K., Dohring, C., and Platzer, M., "Wake Structures Behind Plunging Airfoils: A Comparison of Numerical and Experimental Results," AIAA Paper 1996–0078, January 1996.

[26] Jones, K., Dohring, C., and Platzer, M., "Experimental and Computational Investigation of the Knoller-Betz Effect," *AIAA Journal*, Vol. 36, No. 7, 1998, pp. 1240–1246.

[27] Stanek, M. J. and Visbal, M. R., "Study of the Vortical Wake Patterns of an Oscillating Airfoil," AIAA Paper 89–0554, January 1989.

[28] Theodorsen, T., "General Theory of Aerodynamic Instability and the Mechanism of Flutter," NACA Rept. 496, 1935.